Oxidative coupling of carbon monoxide to dimethyl oxalate: Catalysts design, reaction mechanism and process intensification

Chunzheng Wang, Xianchao Li, Shicheng Yuan, Li Sun, Peng Bai, Lixia Ling, Hailing Guo, Svetlana Mintova

Oxidative coupling of carbon monoxide to dimethyl oxalate: Catalysts design, reaction mechanism and process intensification

Chunzheng Wang,[a,*] Xianchao Li,[a] Shicheng Yuan,[a] Li Sun,[a] Peng Bai,[a] Lixia Ling,[b] Hailing Guo,[a] and Svetlana Mintova[a,c,*]

[a] *Key Laboratory of Heavy Oil Processing, College of Chemistry and Chemical Engineering, China University of Petroleum (East China), Qingdao 266580, China;* [b] *College of Chemistry and Chemical Engineering, Taiyuan University of Technology, Taiyuan 030024, Shanxi, China;* [c] *Normandie Université, Laboratoire Catalyse et Spectrochimie (LCS), ENSICAEN, UNICAEN, CNRS, Caen 14050, France*

[*] Corresponding authors. E-mail addresses: czwang@upc.edu.cn (C. Wang); svetlana.mintova@ensicaen.fr (S. Mintova)

Oxidative coupling of carbon monoxide to dimethyl oxalate: Catalysts design, reaction mechanism and process intensification

Significant efforts have been directed towards the advancement of active and durable Pd-based catalysts for the gas-solid phase oxidative coupling of carbon monoxide (CO) to dimethyl oxalate (DMO). The reaction takes place under moderate conditions with high selectivity above >95% following the C1 chemistry route and converting C1 feedstocks, i.e., CO and methanol (CH_3OH) to DMO product. The inaugural plant capable of processing 200,000 tons annually, was commissioned in 2009, and as of 2023 more than 30 such plants are in operation. Noteworthy attention has been dedicated to enhancing catalytic activity while minimizing the Pd active component, achieved through the construction of efficient nanostructured catalysts. In this review, we highlight the recent advances in the CO oxidative coupling to DMO, particularly focusing on the design of Pd-based catalysts, structure-function relationship, catalytic reaction mechanism and process intensification utilizing structured catalysts. Additionally, an overview addressing challenges and opportunities for future research associated with CO oxidative coupling to DMO is presented.

Keywords: Palladium; Structured catalyst; Reaction mechanism; C1 catalysis; Dimethyl oxalate

1. Introduction

According to the twelve principles of green chemistry, products for the modern world need to be produced in a sustainable, non-hazardous and non-polluting way that integrate the concepts of green chemistry and green engineering [1-3]. However, the traditional production of dimethyl oxalate (DMO) is based on the homogeneous esterification between oxalic acid and methanol, in which mineral acids (e.g., H_2SO_4) are typically used as catalysts and the generated water by-product is removed by the dehydrating agents (e.g., toluene or chloroform) [4,5]. The use of inorganic acid and significant discharge of waste water may lead to the serious equipment corrosion and environmental pollution, conflicting with the 12 principles of green chemistry [6].

C1 chemistry that mainly addresses the transformations of one-carbon molecules such as CO, CO_2, CH_3OH, HCOOH and CH_4, plays an important role in the production of high-value-added chemicals and fuels [7-9]. These C1 molecules are facilely produced from abundant alternative carbon resources such as coal, natural gas, organic waste and biomass [10-12]. The gas-solid phase CO oxidative coupling to DMO converts C1 feedstocks (CO and CH_3OH) to $(COOCH_3)_2$ product [13,14]. This process has been industrialized using the Pd/α-Al_2O_3 catalyst [15,16]. The DMO is closely related with the production of ethylene glycol via hydrogeneration. Commercial ethylene glycol is mainly produced from petroleum-derived ethylene through the hydration of ethylene oxide [17,18]. As an alternative synthesis technology, the transformation of coal to ethylene glycol has received considerable attention due to the potential depletion of petroleum resources [19,20]. As shown in Scheme 1, this technology includes three stages [21-23]: (1) gasification of coal to syngas, (2) CO oxidative coupling to DMO, and (3) hydrogenation of DMO to ethylene glycol. This process was initially proposed by UBE company in the 1970s, and extensively studied by several teams in China, including Ma [24], Xiao et al. [25], Yao and Guo [26], Wang et al. [27], Yuan et al. [28] and Lu et al. [29] in the universities, petrochemical and coal-chemical institutes. The world's first plant capable of 200,000 tons ethylene glycol per year was built in China in 2009 [29]. The total capacity in China has increased dramatically to about 7.0 million tons in 2023, with an average increase of 29% per year [25,31].

The development of high-performance catalyst is a crucial point for the industrialization of the DMO synthesis. In comparison to the first-generation industrial catalyst consisting of 2.0 wt% Pd, the second-generation catalyst is highly active with ultra-low Pd content of 0.13 wt% [32]. The total investment of the process was decreased by about 25%.

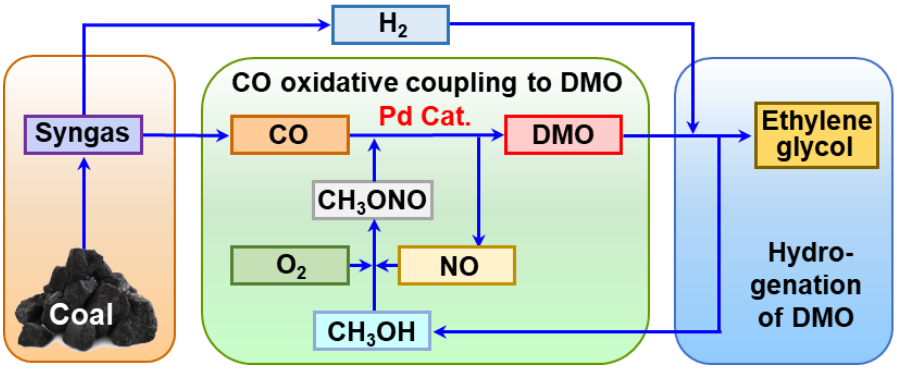

Scheme 1. Schematic presentation of the commercial process of coal to DMO and further to ethylene glycol.

Several reviews related to the DMO, especially catalytic hydrogenation of DMO have been published. Ye et al. [30] demonstrated that the hydrogenation of DMO provided an economical and versatile process for the synthesis of methyl glycolate, ethylene glycol and ethanol over the different catalysts. The synthesis of ethylene glycol via fossil fuels (petroleum, natural gas and coal) and biomass-based resources has been reviewed by Yue et al. [24]. Furthermore, the emergence of non-DMO routes for synthesis of ethylene glycol (EG) such as a two-step process from CO through homogeneous catalysis [33], direct synthesis from syngas [34], photocatalysis (formaldehyde to EG, methanol to EG and methane to EG) and electrocatalysis (CO_2 to EG, CO_2 to EG and ethylene to EG) [35] has gathered significant attention. Wang et al. [36] made an in-depth analysis of the key functional motifs of the Pd-based catalysts that tune the selectivity towards DMO and dimethyl carbonate. The synthesis of DMO and dimethyl carbonate over the Pd catalysts have been studied by Yamamoto [37]. Uchiumi et al. [38] described four Pd-catalysed oxidative reactions with the recycled agent of alkyl nitrite, including dialkyl oxalate, dialkyl carbonate, oxidation of olefins and oxidative carbonylation of olefins.

To our knowledge, a specific review of the CO oxidative coupling to DMO focusing on the catalysts design, catalytic reaction mechanism and process intensification has not been published yet. In this review, the recent advances in the preparation of Pd-based catalysts for the gas-solid phase CO oxidative coupling to DMO are outlined. The main focus is on the development of high-performance catalyst with low Pd content by constructing various nanostructures. The catalytic reaction mechanism including reaction intermediates, rate-determining step and reaction pathways is discussed. Moreover, we concisely retrospect the development of structured catalysts and how the unique structured catalysts enhance the mass/heat transfer is discussed. Finally, a brief perspective on the challenges and future directions of catalysts design for the CO oxidative coupling to DMO is presented.

2. Applications of dimethyl oxalate

DMO is an important platform chemical with useful and versatile chemical properties. As shown in Scheme 2, DMO can be used as feedstock for the synthesis of high-value-added products, including methyl glycolate, ethylene glycol, ethanol, phenol, oxamide, oxalic acid and dimethyl carbonate. The main applications of DMO will be discussed in the following subsections.

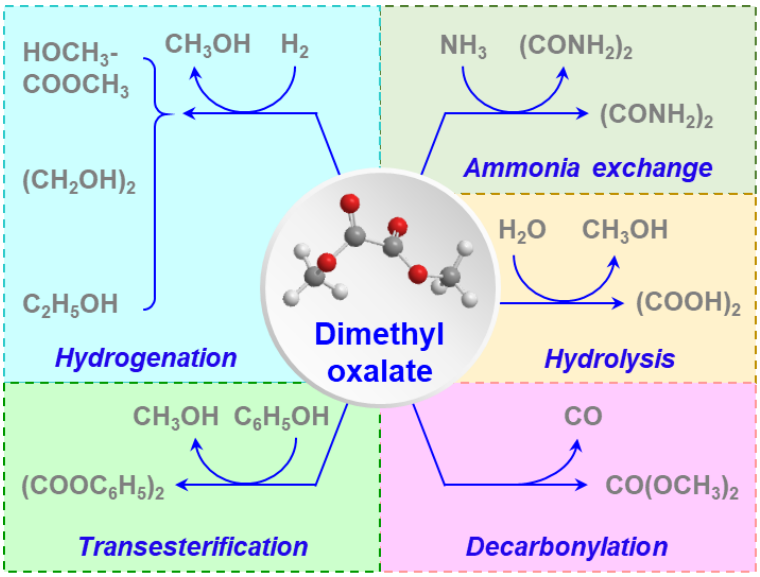

Scheme 2. The main applications of dimethyl oxalate.

2.1. Hydrogenation of DMO to methyl glycolate, ethylene glycol and ethanol

The catalytic hydrogenation of DMO includes three main reactions as shown in Scheme 3: incomplete hydrogenation of DMO to methyl glycolate (Eq. 1), further hydrogenation to ethylene glycol (Eq. 2), and deep hydrogenation to ethanol (Eq. 3). The different active sites of catalysts are responsible for various reaction pathways of DMO hydrogenation. For example, the Ag/SiO_2 [39], Cu/SiO_2 [40] and Cu/Al_2O_3 [41] catalysts exhibited the high yield of 92% methyl glycolate, 95% ethylene glycol and 95% ethanol, respectively through the DMO hydrogenation. Methyl glycolate is a versatile platform compound due to its unique molecular structure comprised of hydroxyl, α-hydrogen and ester groups. Both the ethanol and the ethylene glycol are crucial bulk chemicals in industry. The products of DMO hydrogenation can be tuned efficiently to produce methyl glycolate, ethylene glycol and ethanol, which could decrease the dependence on the petroleum resource to some extent.

$$(COOCH_3)_2 + 2H_2 \rightarrow HOCH_2COOCH_3 + CH_3OH \quad (1)$$

$$(COOCH_3)_2 + 4H_2 \rightarrow (CH_2OH)_2 + 2CH_3OH \quad (2)$$

$$(COOCH_3)_2 + 5H_2 \rightarrow C_2H_5OH + H_2O + 2CH_3OH \quad (3)$$

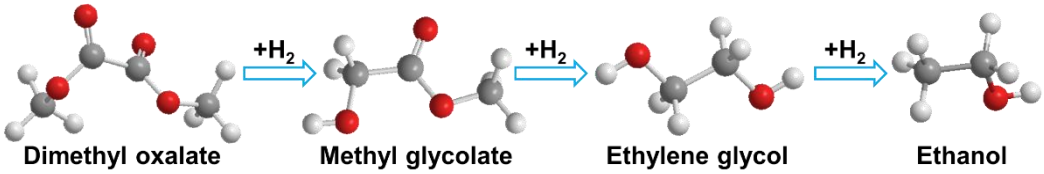

Scheme 3. Schematic presentation of consecutive hydrogenation of DMO $(COOCH_3)_2$ to methyl glycolate ($CH_2OHCOOCH_3$), ethylene glycol $(CH_2OH)_2$ and ethanol (CH_3CH_2OH).

2.2. Transesterification of DMO with phenol

Diphenyl carbonate is an important intermediate used to produce polycarbonate [42]. Diphenyl carbonate was traditionally synthesized from phenol using toxic phosgene. Considerable efforts have been given towards development of novel routes different from the phosgene method [43]. The oxidative carbonylation of phenol and transesterification reactions have been developed as an environmentally benign phosgene-free synthesis approach [44,45]. The transesterification of DMO with phenol to diphenyl oxalate followed by decarbonylation to diphenyl carbonate (Eqs. 4 and 5), is considered as a high atom economy process with low cost and easy separation of products [46,47]. Notably, the high yield (>95) and high selectivity (>99%) has been reported for decarbonylation of diphenyl oxalate to diphenyl carbonate [48].

$$(COOCH_3)_2 + 2C_6H_5OH \rightarrow (COOC_6H_5)_2 + 2CH_3OH \quad (4)$$

$$(COOC_6H_5)_2 \rightarrow CO(OC_6H_5)_2 + CO \quad (5)$$

2.3. Ammonia exchange of DMO to oxamide

Oxamide has a low solubility in water and thus can be used as a slow-release nitrogen fertilizer for agriculture purposes [49,50]. The traditional synthesis of oxamide is based on the oxidation of toxic hydrogen cyanide, HCN [51,52]. Oxamide is still not produced on a large scale due to the high cost and complicated synthesis method [52]. Since DMO has been industrially produced with a low cost, the ammonia exchange of DMO to oxamide is considered as a promising route (Eq. 6). This method has the advantages of high atom efficiency, low cost and moderate reaction conditions [53].

$$(COOCH_3)_2 + 2NH_3 \rightarrow (CONH_2)_2 + 2CH_3OH \quad (6)$$

2.4. Hydrolysis of DMO to oxalic acid

Oxalic acid is the simplest organic diacid with extensive applications, including extraction of rare earth, cleaning of metal surface, printing and dyeing, catalyst preparation and pharmaceutical synthesis [54]. Conventionally, oxalic acid is produced by both carbohydrate and sodium formate methods [55]. The carbohydrate process involves the oxidation of sugar or starch using nitric acid, but it is disadvantaged by a low yield of oxalic acid and high NO_x emissions [55]. Although the sodium formate method provides a high yield of oxalic acid, this process has several disadvantages including long reaction path, difficult recovery of calcium sulfate and high consumption of sulfuric acid [56]. The hydrolysis of DMO to oxalic acid has attracted much interest due to the mass-produced DMO with low cost (Eq. 7) [56]. Recently, this process has been successfully commercialized by Tongliao GEM Chemical Co. Ltd., China (100,000 tons/year) [53].

$$(COOCH_3)_2 + 2H_2O \rightarrow (COOH)_2 + 2CH_3OH \quad (7)$$

2.5. Decarbonylation of DMO to dimethyl carbonate

Dimethyl carbonate (DMC) is considered as an environmentally benign building block due to good biodegradability, high solubility and low toxicity. DMC is widely considered as green solvent, lithium battery electrolyte, additive for fuel oil, reagent for methylation and carbonylation reactions, and raw material for the synthesis of pharmaceuticals, antioxidants and agrochemicals [57,58]. The traditional industrial synthesis of DMC uses toxic phosgene, $COCl_2$ as feedstock, which is gradually being abandoned [59,60]. Therefore, it is of the utmost importance to develop phosgene-free processes for DMC production. The environmentally sustainable approaches for DMC synthesis include the direct/indirect oxidative carbonylation of methanol, transesterification of ethylene or propylene carbonate and methanol, the direct synthesis from carbon dioxide and methanol, the methanolysis of urea, and decarbonylation of DMO [61-64]. Among them, decarbonylation of DMO to DMC is a promising route due to the low-cost and mass-produced DMO. Hao et al. reported that a complete conversion of DMO to DMC via decarbonylation can be achieved based on thermodynamic calculations [65]. Despite the above-mentioned advantages, little research has been dedicated to the decarbonylation of DMO to DMC.

$$(COOCH_3)_2 \rightarrow CO(OCH_3)_2 + CO \quad (8)$$

3. Process of CO oxidative coupling to dimethyl oxalate

Fenton et al. [66] discovered that diethyl oxalate was formed by oxidative carbonylation of ethanol with a $PdCl_2$-$CuCl_2$ catalyst in a liquid phase at 6.9 MPa and 125 ºC (Eq. 9). But this reaction cannot proceed in the presence of water, and thus the excess of ethyl orthoformate must be used as dehydrating agent which is an essential drawback of the method due to high cost [38,66].

$$2CO + 2CH_3CH_2OH + 0.5O_2 \rightarrow (COOCH_2CH_3)_2 + H_2O \quad (9)$$

To avoid the use of expensive ethyl orthoformate, methyl nitrite was employed as an effective recycling agent. As shown in Scheme 4, the indirect oxidative carbonylation of methanol to DMO is a chemical-looping and two-step process [67]. The first step is the Pd-catalysed CO oxidative coupling to DMO from methyl nitrite and CO (Eq. 10). The second step is the non-catalytic regeneration of methyl nitrite from methanol, oxygen and recycled nitric oxide (Eq. 11). Both methyl nitrite and nitric oxide can be fully recycled in the process. The first step can be operated in a fixed-bed reactor under moderate reaction conditions. Notably, the water by-product can be easily removed in the second step (Eq. 11) and thus the DMO synthesis is conducted in an anhydrous system in the first step (Eq. 10) [63,67]. The overall reaction results in a self-closing and environmentally-benign process, converting C1 feedstocks of CH_3OH and CO to $(COOCH_3)_2$ product (Scheme 4).

$$2CH_3ONO + 2CO \rightarrow (COOCH_3)_2 + 2NO \quad (10)$$

$$2NO + 2CH_3OH + 0.5O_2 \rightarrow 2CH_3ONO + H_2O \quad (11)$$

$$2CO + 2CH_3OH + 0.5O_2 \rightarrow (COOCH_3)_2 + H_2O \quad (12)$$

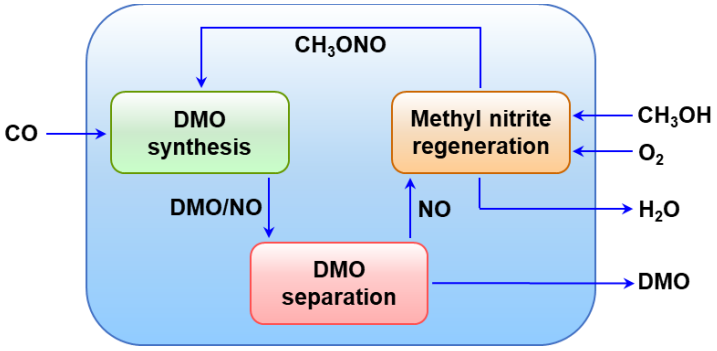

Scheme 4. Schematic presentation of the commercial indirect oxidative carbonylation of methanol to DMO process.

It should be noted that the recycling agent of methyl nitrite is responsible for the high activity and selectivity in the indirect oxidative carbonylation of methanol to DMO (Scheme 4). Methyl nitrite is a reactive molecule due to the weak CH_3O–NO bond (176 kJ mol^{-1}) [68]. The dissociation of methyl nitrite on the Pd-based catalysts is widely considered as the first step for the DMO formation [69,70]. The boiling point of methyl nitrite is only –12 ºC, which is beneficial for the gas-solid phase reaction. However, the experimental and theoretical data revealed a potential explosion risk of methyl nitrite [71]. To prevent an explosion in the commercial reactors, the concentration of methyl nitrite should be kept below 20%. Moreover, methyl nitrite can be easily synthesized by dropping H_2SO_4 into an aqueous solution of CH_3OH and $NaNO_2$ at laboratory scale (Eq. 13) [72]. The industrial synthesis of methyl nitrite is from methanol, oxygen and recycled nitric oxide as stated previously (Eq. 11).

$$2NaNO_2 + 2CH_3OH + H_2SO_4 \rightarrow 2CH_3ONO + Na_2SO_4 + 2H_2O \quad (13)$$

4. CO oxidative coupling to dimethyl oxalate: Pd-based catalysts

Pd-based catalysts play a crucial role in the process of coal to ethylene glycol. The second-generation industrial catalyst had a much lower Pd content of 0.13 wt% in comparison to the first-generation industrial catalyst of 2.0 wt% Pd. The total cost was decreased by about 25% using the second-generation industrial catalyst [32]. The effects of the active component (Pd), catalyst supports and promoters have been intensively investigated. Table 1 summarizes various types of Pd-based catalysts used for the CO oxidative coupling to DMO.

Table 1 Pd-based catalysts used for the CO oxidative coupling to DMO.

No.	Catalyst	Pd (wt%)	CO/CH_3O NO	GHSV (L kg^{-1} h^{-1})	T (ºC)	CO conv.	DMO sel. (%)[a]	TOS (h)[b]	Ref.

			(mole)			(%)[a]			
1	Pd/Al_2O_3	0.5	1.3	2160	110	39	96	480	[73]
2	$Pd/\alpha\text{-}Al_2O_3$	0.1	2.0	3000	120	42	95	---	[74]
3	$Pd/\alpha\text{-}Al_2O_3$	0.37	1.4	3000	130	---	99	100	[26]
4	$Pd/\alpha\text{-}Al_2O_3$	0.5	1.0	2000	110	---	97	---	[38]
5	Industrial $Pd/\alpha\text{-}Al_2O_3$	2.0	1.4	3000	130	34	95	---	[32]
6	$Pd/\alpha\text{-}Al_2O_3$	0.13	1.4	3000	130	62	97	100	[32]
7	Pd/Mg-ZnO	0.5	1.4	3000	130	67	98	100	[75]
8	Pd/MgO	0.42	1.4	3000	130	63	97	120	[76]
9	Pd/TiO_2	0.43	1.4	3000	130	26	90	---	[76]
10	$Pd/\gamma\text{-}Al_2O_3$	0.41	1.4	3000	130	20	88	---	[76]
11	Pd/active-carbon	0.42	1.4	3000	130	15	89	---	[76]
12	Pd/active-carbon	0.5	1.0	2000	110	---	95	---	[37]
13	$Pd/\gamma\text{-}Al_2O_3$	0.5	1.0	2000	110	---	93	---	[38]
14	Pd/SiO_2	0.5	1.0	2000	110	---	94	---	[37]
15	Pd/carbon-nanofiber	1.0	1.3	4500	120	71	99	---	[77]
16	$Pd\text{-}CeO_2/\alpha\text{-}Al_2O_3$	0.8	1.2[c]	1200	140	65	93[d]	72	[78]
17	$Pd\text{-}CeO_2/\alpha\text{-}Al_2O_3$	1.0	1.2	3500	140	75	---	---	[79]
18	$Pd\text{-}Fe/\alpha\text{-}Al_2O_3$/Cordierite	1.0	1.3	2000	120	60	96	---	[80]
19	$Pd\text{-}Fe/\alpha\text{-}Al_2O_3$/Cordierite	1.0	1.3[c]	2500	120	36	93[d]	---	[81]
20	Pd/ns-	0.25	1.4	3000	150	66	94	200	[29]

	AlOOH/Al-fiber								
21	Pd/AlOOH/Al-fiber	0.26	1.4	3000	150	67	96	150	[82]
22	PdC_x/AlOOH/Al-fiber	0.25	1.4	20000	150	67	95	150	[83]
23	Pd/α-Al_2O_3/Al-fiber	0.25	1.4	20000	150	58	95	150	[84]
24	Np-Pd/Al-fiber	0.28	1.4	3000	150	55	95	150	[85]
25	Pd/HKUST-1	5.81	1.6	3000	130	60	91	100	[86]
26	Pd/ZnTi-LDH	0.06	1.4	3000	130	65	96	100	[87]
27	Pd/Zn-Al-O	0.53	1.4	3000	130	64	98	---	[88]
28	Pd/Nb_2O_5	1.0	1.6	3000	130	63	93	50	[89]
29	Pd/MgO/γ-Al_2O_3	0.4	1.1	4000	125	48	94	100	[90]
30	Pd/α-Al_2O_3- ball-milling	1.0	1.4	12000	125	35	99	100	[91]
31	Pd/UiO-66	0.9	1.6	3000	130	30	89	---	[92]

[a] CO conversion, and DMO selectivity based on the CO or CH_3ONO reactant.

[b] Time on steam (TOS).

[c] The CH_3CH_2ONO is used instead of CH_3ONO, and thus the $(COOCH_2CH_3)_2$ is formed through the reaction ($2CH_3CH_2ONO + 2CO \rightarrow (COOCH_2CH_3)_2 + 2NO$).

[d] The selectivity of $(COOCH_2CH_3)_2$ instead of $(COOCH_3)_2$.

4.1. Active Pd component of catalysts

Palladium has been demonstrated to be the most active component for the CO oxidative coupling to DMO [93,94]. However, the industrial Pd/α-Al_2O_3 catalyst needs a relatively high Pd loading of 2 wt% thus affecting the catalyst price [32]. Therefore, lowering the Pd content of the catalysts by enhancing the activity is an ongoing avenue

of research. The recent trends in the development of low-Pd-content catalysts are summarized below.

4.1.1. Control of Pd size

In the heterogeneous catalysis, the reactants interact with the surface-active sites while the underlying atoms are not accessible to the reactants in the reaction process [95]. Hence, reducing the size of the active component is a commonly used method for producing more active sties [96]. Peng et al. proposed a plausible Cu^{2+}-assisted growth mechanism of Pd nanoparticles during the catalyst preparation (Scheme 5) [32]. The introduction of Cu^{2+} was found to inhibit the reduction of $PdCl_4^{2-}$ and changed the growth kinetics of Pd nanoparticles. The Pd/α-Al_2O_3 catalyst with Cu^{2+}-assisted preparation showed an average size of Pd nanoparticles of 2.7 nm with a Pd dispersion of 19.8%, while the catalyst without Cu^{2+} had a size of 11.6 nm with a dispersion of 5.4%. This new Pd/α-Al_2O_3 catalyst with an ultra-low Pd loading of only 0.13 wt% exhibited high activity and stability for the DMO synthesis (Table 1) [32]. Wang et al. found that the Pd dispersion was sensitive to the thickness of boehmite (AlOOH) nanosheets support (Scheme 6) [82]. The best-performing catalyst was the one using the thinnest AlOOH nanosheet of 26 nm loaded with a Pd content of 0.26 wt%. This catalyst showed high CO conversion of 67% and DMO selectivity of 96%, that maintained for at least 150 h (Table 1). The anchoring of metal atoms onto surface oxygen vacancies is an effective method for preparation of single-atom catalysts [97]. Ling et al. [98] reported on Pd_n (n = 1, 4 and 6) clusters anchored on single-vacancy graphene with high activity and selectivity for the DMO synthesis by density functional theory (DFT) calculations. They also found that Pd clusters loaded on TiO_2 with an

oxygen vacancy (TiO_2-v) had a remarkable influence on the catalytic performance following the order of Pd_4/TiO_2-v > Pd_6/TiO_2-v > Pd_2/TiO_2-v > Pd_3/TiO_2-v [99].

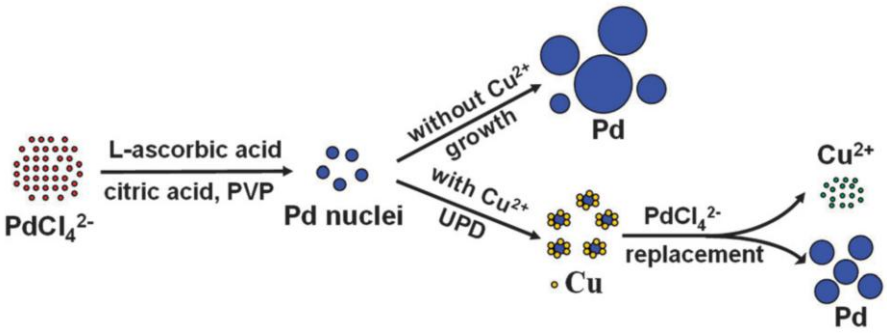

Scheme 5. Schematic diagram of catalyst with Pd nanoparticles prepared in the presence of Cu^{2+} ions. (Reproduced with permission from ref.[32]. Copyright 2013 Royal Society of Chemistry).

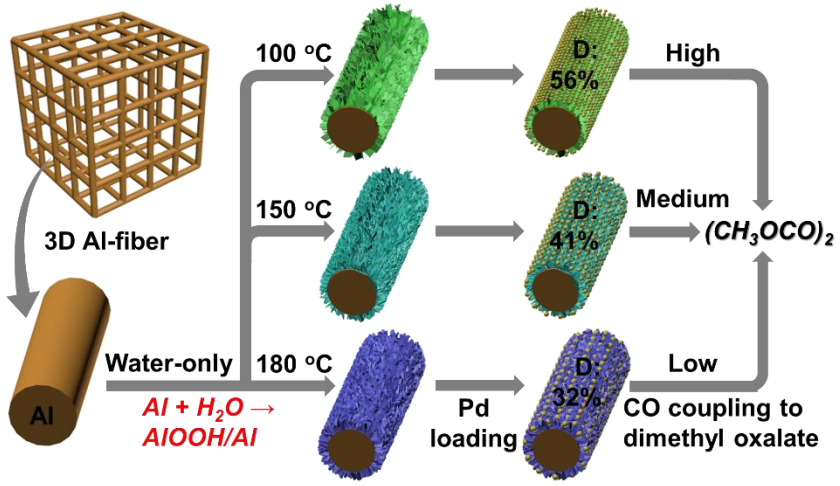

Scheme 6. Schematic diagram representing the effect of boehmite (AlOOH) morphology on the Pd dispersion over the Pd/AlOOH/Al-fiber catalyst. (Reproduced with permission from ref.[82]. Copyright 2017 American Chemical Society).

4.1.2. Control of Pd facet

Studies on single crystal surfaces have revealed that different crystal planes exhibit diverse catalytic performance [100]. The possibility to enhance the catalyst activity by synthesizing shape-controlled nanomaterials has been reported [101]. Xu et al. synthesized the mono-dispersed Pd nanocrystals with exposed (111) or (100) facets through preferentially oriented facet growth method (Figure 1). They found that the (111) facets of Pd nanocrystals are the active planes for the DMO synthesis [26]. Five kinds of Pd nanoparticles including concave cubes, nano-cubes, truncated octahedral, decahedra and icosahedra shapes were prepared by a liquid-phase reduction approach [102]. It was demonstrated that the Pd (111) facets were responsible for the high activity of DMO synthesis, as the result of promoted adsorption of bridged CO [102]. Wang et al. reported the preparation of nanoporous palladium (np-Pd) catalyst on microfibrous-structured Al-fibers for the DMO synthesis (Figure 2) [85]. The catalyst of np-Pd/Al-fiber was fabricated by a spontaneous deposition of Pd^{2+} and Al metal ($2Al + 3Pd^{2+} \rightarrow 2Al^{3+} + 3Pd$). The catalyst with a Pd loading of 0.28 wt% showed four times higher intrinsic activity (i.e., turnover frequency) than the Pd/α-Al_2O_3 catalyst.

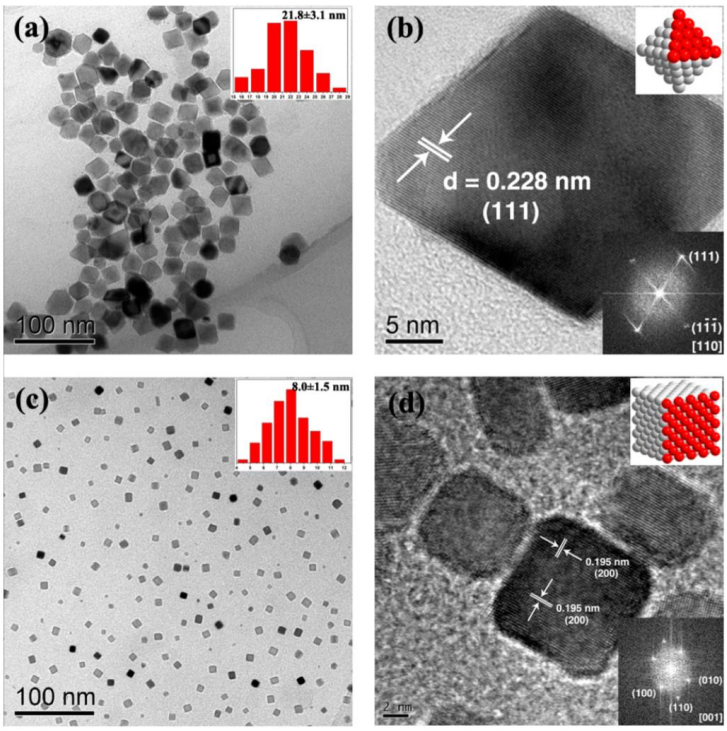

Figure 1. TEM images of Pd (a,b) nano-polyhedra and (c,d) nano-cubes. *Insets* of (a,c) are the corresponding size distributions of Pd. *Insets* of (b,d) show the corresponding FFT patterns and models. (Reproduced with permission from ref.[26]. Copyright 2013 American Chemical Society).

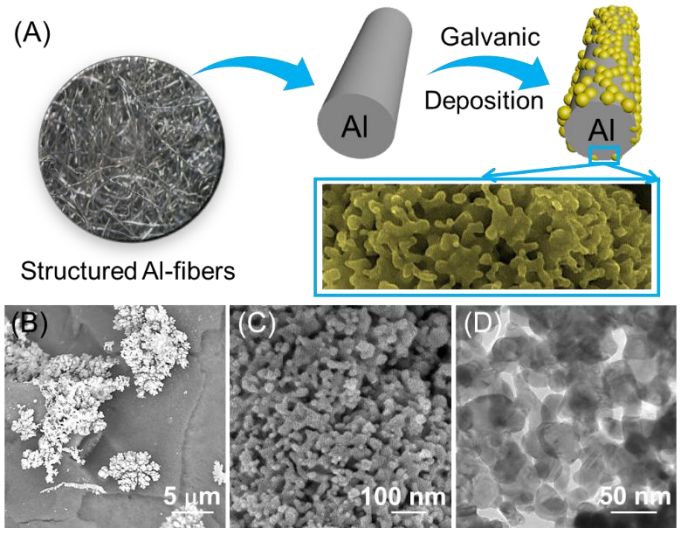

Figure 2. (A) Schematic illustration for the preparation of np-Pd/Al-fiber catalyst (np: nanoporous). (B, C) SEM and (D) TEM images of the np-Pd/Al-fiber catalyst. (Reproduced with permission from ref.[85]. Copyright 2019 Elsevier).

4.1.3. Control of Pd structure

The preparation of highly active catalysts with low Pd content by constructing novel structures has been reported [103,104]. A high-performance and low Pd-containing catalyst was prepared by carburizing a Pd/AlOOH/Al-fiber (0.25 wt% Pd) using ethylene gas [83]. The O_2-TPO results suggested that an amorphous carbon was 'physically' attached on the surface of Pd nanoparticles (a peak at 239 ºC in the O_2-TPO). While the peaks at 325 and 450 ºC in the O_2-TPO implied that the carbon on the Pd nanoparticles resulted in the formation of surface PdC_x species (Figure 3) [105,106]. These PdC_x species improved the turnover frequency (TOF) of the DMO synthesis [83]. An egg-shelled Pd/α-Al_2O_3 pellet catalyst was prepared by adjusting the pH of the precursor solution [107]. It was reported that the Pd active component should be placed as a thin layer at the external surface of the pellet. The optimal Pd loading and impregnated depth of the catalyst were 0.10 wt% and 16 μm, respectively. In addition, the paired- and isolated-Pd^{2+} centers have been embedded in the MOFs framework of HKUST-1 type material [86]. The synthesized paired-Pd^{2+}/HKUST-1 catalyst showed a high DMO selectivity of 91%, while the isolated-Pd^{2+}/HKUST-1 catalyst exhibited a high dimethyl carbonate selectivity of 85%. This suggested that the DMO was formed from the neighboring $COOCH_3$ species adsorbed on the paired-Pd^{2+} centers through the Langmuir-Hinshelwood mechanism, while the dimethyl carbonate was generated by the gaseous CH_3ONO and $COOCH_3$ species adsorbed on the isolated-Pd^{2+} centers through the Eley-Rideal mechanism.

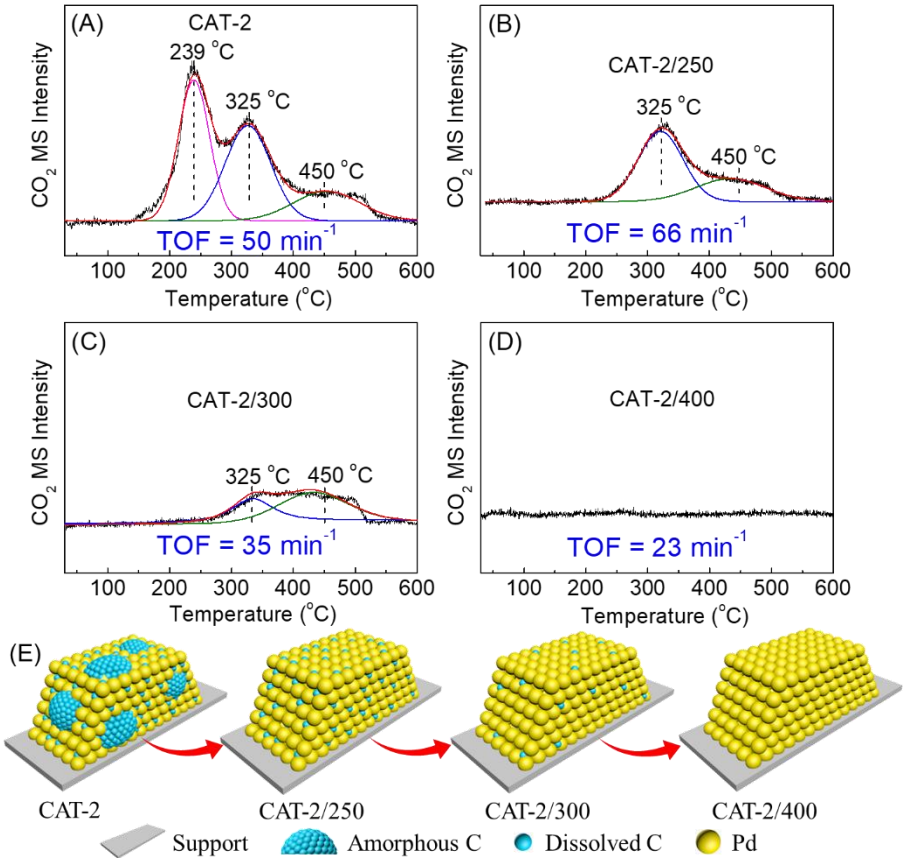

Figure 3. The O_2-TPO profiles of the fresh PdC_x/AlOOH/Al-fiber catalyst (CAT-2) (A), and the CAT-2 samples after post calcination in air at (B) 250 ºC: CAT-2/250, (C) 300 ºC: CAT-2/300 and (D) 400 ºC: CAT-2/400. (E) Schematic illustration of the evolution behaviour of carbon species after calcination. Note: the mass spectrometer (MS) intensity at m/e 44 represents the CO_2. (Reproduced with permission from ref.[83]. Copyright 2019 Elsevier).

Furthermore, Han et al. reported that both Pd single-atom-doped Cu (111) and Ag (111) surfaces exhibited higher activity than pure Pd (111) based on DFT calculations [108,109]. It is worth noting that both Cu (111) and Ag (111) participated in the adsorption of CO and CH_3ONO reactants and the formation of DMO. Based on the reaction mechanism conducted by DFT, a Cu monolayer supported on carbon-terminated $Mo_2C(001)$ ($Cu_{ML}/Mo_2C(001)$-C) exhibited high activity for DMO synthesis due to the synergistic effect between the Cu monolayer and the $Mo_2C(001)$ [110].

Therefore, it is reasonable to consider elements close to Pd in the periodic table, such as Fe, Co, Ni, Cu, Zn, and Ag, as potential candidates for non-noble metal doping catalysts to replace the high-cost Pd catalysts. However, palladium is widely considered to be the most active component for DMO synthesis. The effectiveness of tuning the Pd active sites can be ranked in the following order: the control of Pd size > the control of Pd structure > the control of Pd facet.

4.2. Catalyst supports

4.2.1. Types of catalyst support

Acidity of catalyst support is considered to be harmful to DMO formation. It was suggested that acid sites can accelerate the decomposition of methyl nitrite reactant (Eq. 14), which is a parallel competing reaction to the DMO formation [111]. Uchiumi et al. reported the decomposition of methyl nitrite on acid sites with a very low activation energy of 52.7 kJ mol^{-1} based on Gaussian calculations [38]. The effect of alkyl nitrite decomposition on the catalytic performance was also reported by Li et al. [112]. By combining experimental and DFT studies it was found that the ethyl nitrite decomposed more easily than the methyl nitrite using the same Pd-Fe/α-Al_2O_3 catalyst. Yamamoto showed that the Pd supported on active carbon, SiO_2, SiO_2-Al_2O_3, NaY exhibited lower activity than on α-Al_2O_3 support [37]. The high activity of α-Al_2O_3 support may be attributed to its neutral property and the optimal interaction between Pd and the support [113,114].

$$4CH_3ONO \rightarrow CHOOCH_3 + 2CH_3OH + 4NO \quad (14)$$

The catalytic activity of Pd supported catalysts is strongly dependent on the type of supports, and thus it is essential to consider the development of new supports for the CO oxidative coupling to DMO [115]. Peng et al. firstly found that the basic MgO could

be employed as an appropriate support for DMO synthesis [76]. CO conversion increased from 43% to 69% with increasing the Pd loading from 0.1 wt% to 2.0 wt% on the MgO support, as the result of the increased and accessible surface-active sites. Yang et al. demonstrated that a Pd/MgO/γ-Al_2O_3 catalyst exhibited 3 times higher space time yield than that of Pd/γ-Al_2O_3 [90]. The γ-Al_2O_3 surface was covered by 30 wt% MgO layer, which increased the surface basicity and enhanced the interactions between Pd and MgO. Wang et al. reported the use of boehmite (AlOOH) nanosheet support with a low Pd loading (0.25 wt%), and the as-obtained Pd/AlOOH/Al-fiber catalyst showed high activity and stability for DMO synthesis [94]. The AlOOH nanosheets on the Al-fiber were prepared with the aid of oxidation reaction between Al metal and water ($2Al + 4H_2O \rightarrow 2AlOOH + 3H_2$). After the oxidation of Al metal, the AlOOH nanosheets were formed and disorderedly aligned to a homogeneous honeycomb-like shell along with the Al-fiber core (Figure 4). The method for preparation of AlOOH nanosheets can be applied to various shaped Al substrates, including powders, foams, wires, foils, tubes and microchannels (Figure 5) [94]. The results of reaction pathway, energy barrier and microkinetic analysis deduced from DFT calculations, predicted that the Pd supported on defective graphene, TiO_2 with oxygen vacancy, C_2N motif, and N-doped or oxidized graphene are effective catalysts for the DMO synthesis [98,99,116-118].

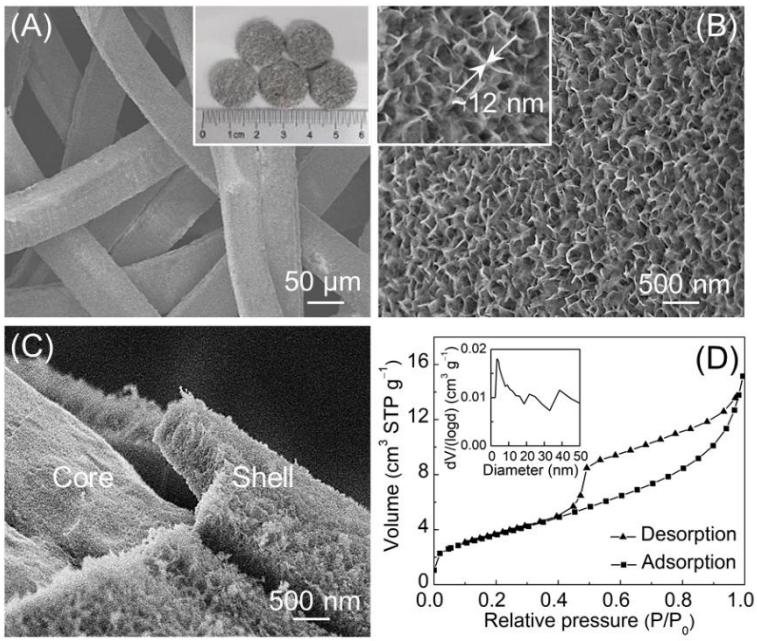

Figure 4. (A) Low-magnification SEM image, showing a characteristic irregular 3D open network (*inset*: optical photograph). (B) High-magnification SEM image, showing honeycomb-like morphology of boehmite (AlOOH) nanosheets (*inset*: thickness of nanosheets). (C) SEM image of core(Al-fiber)-shell(AlOOH) material. (D) N_2 adsorption-desorption isotherm of core(Al-fiber)-shell(AlOOH) material (*inset*: Barrett-Joyner-Halenda (BJH) mesopore size distribution). (Reproduced with permission from ref.[94]. Copyright 2015 Royal Society of Chemistry).

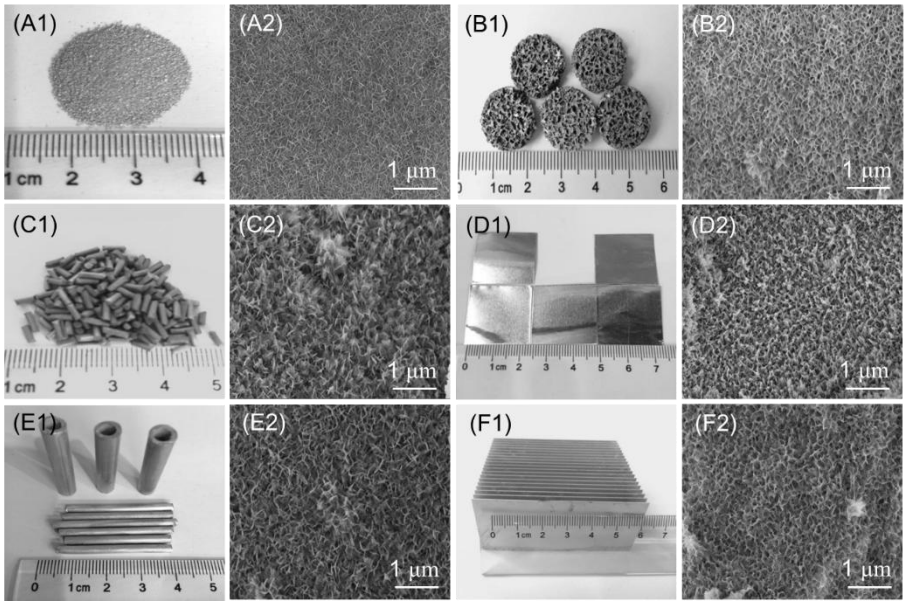

Figure 5. The optical photographs and SEM images of (A1,A2) Al powders, (B1,B2) Al foams, (C1,C2) Al wires, (D1,D2) Al foils, (E1,E2) Al tubes and (F1,F2) Al microchannels after the oxidation of Al metal in steam flow at 120 ºC for 6 h. (Reproduced with permission from ref.[94]. Copyright 2015 Royal Society of Chemistry).

4.2.2. Interactions between active Pd and support

Although the nature of metals plays an important role in the catalytic performance, the interactions of the supports with the nanoparticles are considered as an integral part in controlling the activity and stability of metal supported catalysts [119-121]. A nearly linear relationship between the turnover frequency (TOF) and the amount of hydroxyls on the Pd/AlOOH/Al-fiber catalysts has been found (Figure 6) [29]. All four catalysts considered for establishing the relationship possessed identical Pd loading, similar Pd nanoparticle size and Pd oxidation state while contained different hydroxyl groups. Based on this study, it was suggested that the Pd-hydroxyl interactions were responsible for the intrinsic activity improvement. *In situ* diffuse reflectance infrared

Fourier transform spectroscopy (DRIFTS) experiments further confirmed that hydroxyl groups promoted the adsorption of bridged CO, which is an active intermediate for the DMO formation [29,70]. In addition, a high-surface-area α-Al_2O_3 rich in hydroxyls was prepared by ball-milling approach [91]. The surface hydroxyls inhibited the aggregation of Pd nanoparticles and enhanced the interactions between Pd and α-Al_2O_3 support. The optimal Pd/α-Al_2O_3-B800 catalyst exhibited the highest DMO space time yield of 2663 g L^{-1} h^{-1} and 99.8% DMO selectivity.

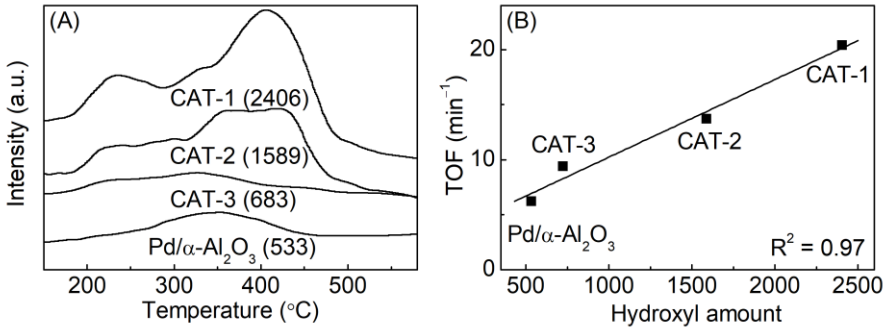

Figure 6. (A) The TPD profiles of dehydroxylation (the data in parentheses show the peak areas from 150 ºC to 580 ºC) and (B) the linear relationship between the hydroxyl amount (TPD peak areas) and TOFs of the four catalysts. (Reproduced with permission from ref.[29]. Copyright 2016 Elsevier).

A Pd/ZnO catalyst with high CO conversion of 67% and DMO selectivity of 98% at 130 ºC was also presented by Peng et al. (Figure 7) [75]. The Pd/ZnO catalyst gradually deteriorated within 100 h (Figure 7). In order to ameliorate the problem, Mg^{2+} ions were introduced into the ZnO support. Interestingly, the Pd catalyst supported on the Mg^{2+}-doped ZnO (Pd/Mg-ZnO) was found to be stable for at least for 100 h (Figure 7). The HAADF-STEM-EDS elemental mapping showed that the Zn and Mg were homogeneously distributed on the Mg^{2+}-doped ZnO support. Fourier transform infrared spectroscopy (FTIR), and H_2-temperature-programmed reduction (H_2-TPR) results

further indicated that the Mg^{2+} ions resulted in a strong metal-support interaction caused by electron transfer from the ZnO support to the Pd nanoparticles, thus resulting in excellent resistance of Pd to sintering.

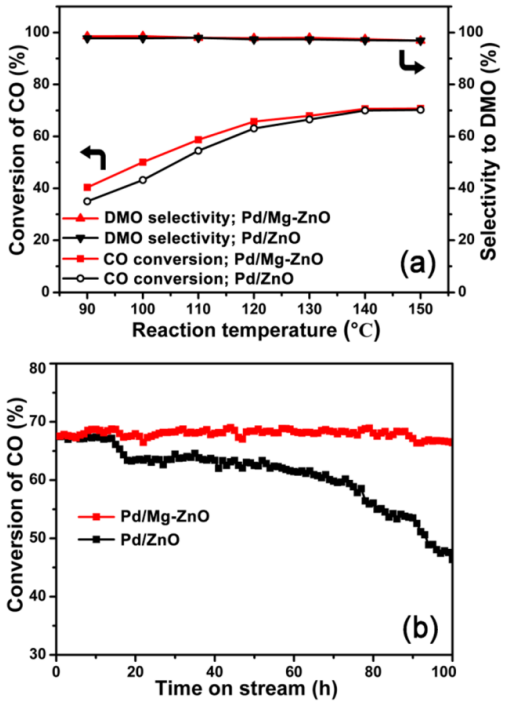

Figure 7. (a) CO conversion and DMO selectivity on the Pd/ZnO and Pd/Mg-ZnO catalysts as a function of reaction temperature for the CO oxidative coupling to DMO. (b) Lifetime test of Pd/ZnO and Pd/Mg-ZnO catalysts at 130 ºC. (Reproduced with permission from ref.[75]. Copyright 2015 American Chemical Society).

Ultrathin ZnTi-layered double hydroxide (LDH) nanosheets with abundant oxygen defects were prepared and used to anchor Pd clusters [87]. The Pd/ZnTi-LDH catalyst with rich oxygen defects showed excellent stability for the DMO synthesis, while the Pd/ZnAl-LDH catalyst with low oxygen defects exhibited relatively poor stability. The interfacial electron transfer was 0.62 e on the Pd/ZnTi-LDH catalyst and only 0.08 e on the Pd/ZnAl-LDH catalyst. It was suggested that the Pd clusters possibly occupied the oxygen defects and were bonded with Zn and Ti atoms, thus forming a

metal-metal bond on the ZnTi-LDH nanosheets. The interfacial electron transfer via defect induction was responsible for the high stability (Scheme 7). In addition, hierarchical Nb_2O_5 microspheres [89] and spinel-like Zn-Al-O oxide [88] rich in oxygen defects were also prepared and used for the stabilization of Pd clusters. The electron transfer between Pd and Nb species led to the formation of interfacial Pd-NbO_x sites on the Pd/Nb_2O_5 catalyst, which contributed to the high catalytic performance for the DMO synthesis.

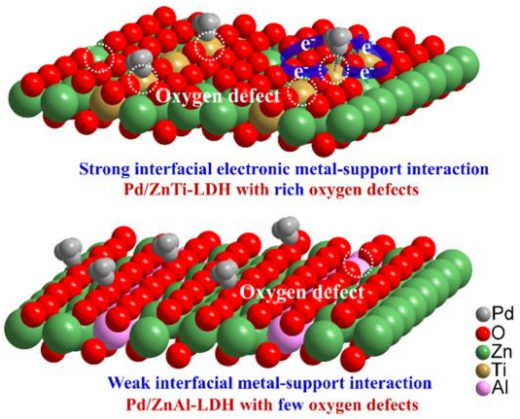

Scheme 7. Schematic presentation of the metal-support interactions via introduction of oxygen defects. (Reproduced with permission from ref.[87]. Copyright 2021 American Chemical Society).

Recently, Pd nanoparticles of about 2 nm were incorporated into the metal-organic frameworks (MOFs) UiO-66-X (X = –H, $–NO_2$, $–NH_2$), forming Pd@UiO-66-X catalyst (Figure 8) [92]. The Pd@UiO-66-X catalyst exhibited high selectivity of dimethyl carbonate of 99%, while the Pd nanoparticles on the surface of UiO-66 (Pd/UiO-66) showed high DMO selectivity of 89% (Scheme 8). It was revealed that the microenvironment of Lewis acid sites could affect the interface between Pd and Zr-oxo clusters, and thus Pd location relative to the UiO-66 support was closely related to the product selectivity.

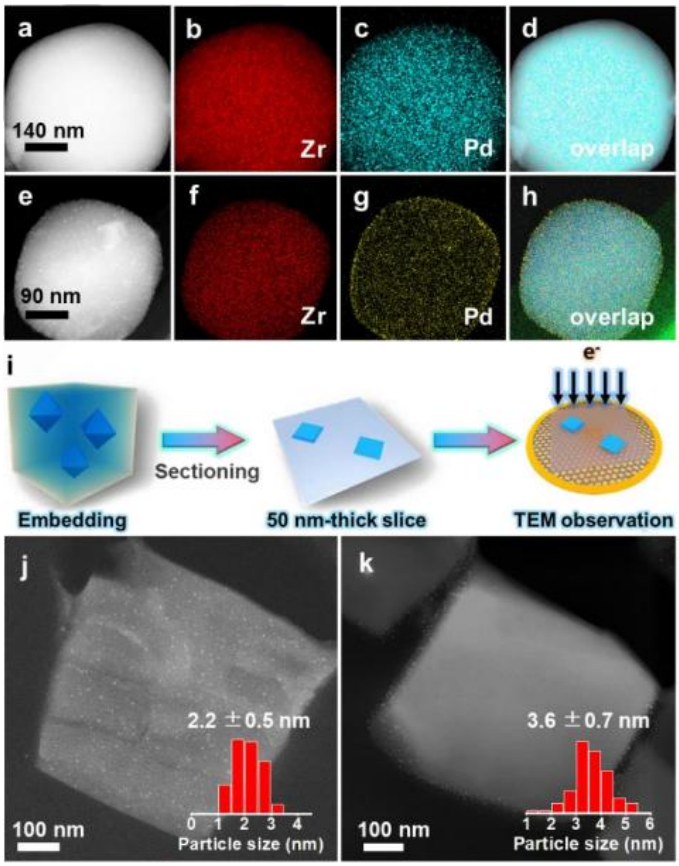

Figure 8. The HAADF-STEM images and corresponding elemental mapping of (a–d) Pd@UiO-66 and (e–h) Pd/UiO-66; (i) Schematic diagram for slicing up of resin-embedded catalysts; (j) sliced Pd@UiO-66 and (k) sliced Pd/UiO-66 catalysts. (Reproduced with permission from ref.[92]. Copyright 2023 Wiley-VCH).

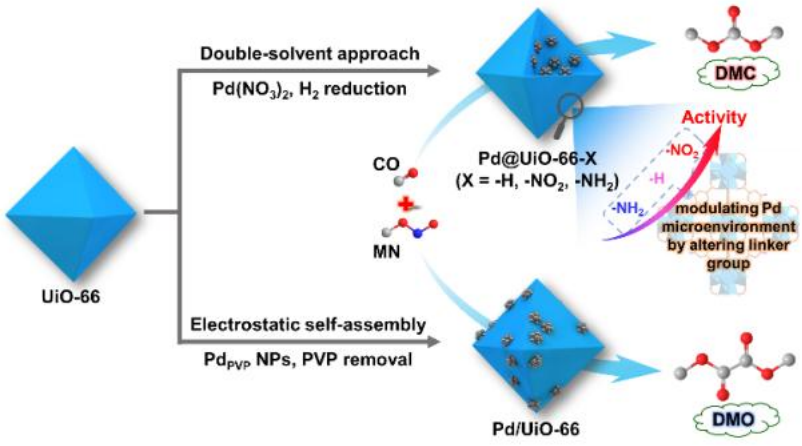

Scheme 8. Schematic diagram for different catalytic performance on the syntheses of DMO and dimethyl carbonate (DMC) over the Pd@UiO-66-X (X = –H, $–NO_2$, $–NH_2$) and Pd/UiO-66 catalysts. (Reproduced with permission from ref.[92]. Copyright 2023 Wiley-VCH).

4.3. Catalyst promoters

The promoter by itself has little or no catalytic effect, while interacting with the active component the promoter would alter the performance of the catalysts [122,123]. For example, Pd/α-Al_2O_3 catalyst with an iron promoter showed high catalytic activity and was stable for 1000 h [124]. The results suggested that the iron promoter was preferentially dispersed on the α-Al_2O_3 support, and the active component Pd preferred to locate on the FeO layer. In summary, the sandwich-like Pd/FeO/α-Al_2O_3 structure was formed. Additionally, Zhao et al. confirmed that the Fe promoter increased the dispersion of Pd [125]. The Pd loading was reduced from 1.0 wt% to 0.3 wt% without lowing the activity of the catalysts. It was found that the CeO_2 promoter not only improved the Pd dispersion, but also enriched the Pd concentration on the catalysts surface [79]. The adsorption of CO on the Pd-CeO_2/α-Al_2O_3 catalyst was stronger than that on the Pd/α-Al_2O_3 catalyst, which played an important role in the DMO formation. Another study reported on the Mg promoter added into the Pd/ZnO catalyst for the DMO synthesis [75]. It was demonstrated that a small portion of Mg^{2+} ions promoter was incorporated into the lattice of the ZnO support. The introduction of Mg^{2+} ions caused the electron transfer from the ZnO support to Pd nanoparticles that restrained the Pd sintering and thereby enhanced the catalysts stability [75]. Zhao et al. based on DFT calculations suggested that the Cu promoter improved both the conversion and

selectivity of the Pd/Graphdiyne catalyst [27]. The decreased charge density of Pd clusters was found to be responsible for the enhanced DMO selectivity.

5. CO oxidative coupling to dimethyl oxalate: reaction mechanism

Understanding the reaction mechanism is of great importance for the rational design and fine tuning of catalysts [126-128]. Although the CO oxidative coupling to DMO has been successfully industrialized, the reaction mechanism is still open for debate. The reaction intermediates, rate-determining step, reaction pathway and kinetics will be presented in the following subsections.

5.1. Reaction intermediates

The dissociation of methyl nitrite (CH_3ONO) on the Pd-based catalysts is considered as the first step for DMO formation. The dissociation adsorption of CH_3ONO formed the CH_3O* and NO* species (*, a surface site) [93]. As shown in Figure 9, the CH_3O* species were detected by DRIFTS spectroscopy; the CH_3ONO adsorption suggested that the formed NO* desorbed directly or partially migrated to the support and generated the nitrates and nitrites [129,130]. Further the catalytic dissociation of CH_3ONO to CH_3O* and NO* was proved by DFT; a low activation energy of 0.03 eV was calculated in the presence of catalyst, while without catalysts the activation energy is as high as 1.91 eV [131]. Other DFT calculations approved that the dissociation adsorption of CH_3ONO resulted in the formation of CH_3O* species [132,133].

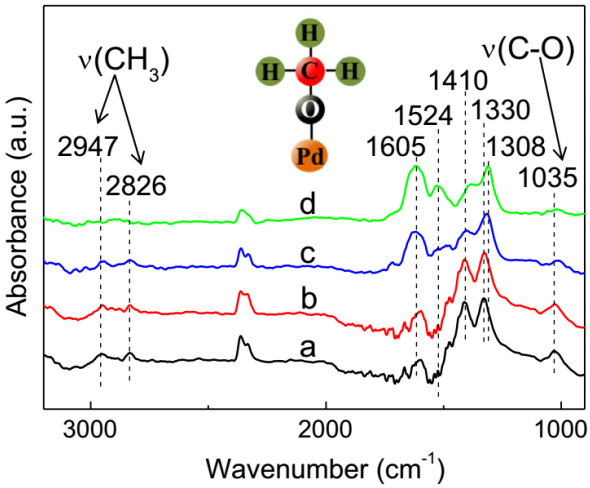

Figure 9. DRIFTS spectra of methyl nitrite (CH_3ONO) reactant adsorbed on the Pd/AlOOH/Al-fiber catalyst at different temperatures: (a) 35, (b) 50, (c) 100 and (d) 150 ºC. The bands at 2947, 2826 and 1035 cm^{-1} were attributed to the stretching vibration (ν) of CH_3 and C–O corresponding to the OCH_3 species. The bands at 1605, 1524, 1410, 1330 and 1308 cm^{-1} were assigned to the alumina bound nitrates and nitrites. (Reproduced with permission from ref.[93]. Copyright 2016 Elsevier).

Carbon monoxide is not only a common probe molecule but also the reactant for DMO synthesis. Two main categories of carbonyls were identified on Pd^0 characterized by the CO stretching vibrations: linear CO species in the 2130–2000 cm^{-1} region and bridged CO species in the 2000–1800 cm^{-1} region [134,135]. There is still ongoing discussion whether the linear or bridged CO takes part in DMO formation. Ji et al. revealed that CO adsorption generated linear and bridged CO species on the Pd/α-Al_2O_3 catalyst, but only the bridged CO participated in the DMO synthesis [70]. Wang et al. observed that the bridged CO was consumed by the pulsed CH_3ONO reactant at 100 ºC and 150 ºC on the Pd/AlOOH/Al-fiber and Pd/α-Al_2O_3 catalysts, respectively (Figure 10) [29]. They found that the CO conversion was related to the adsorption of bridged CO. In conclusion, the linear CO was reported as a spectator and only bridged CO was a

participant for the CO oxidative coupling to DMO. In addition, Gao et al. suggested that the active linear CO easily inserted metal ion-alkoxyl ion bond, since the adsorption of linear CO was weaker than that of bridged CO [69]. Additionally, the CO adsorption on the Pd/α-Al_2O_3 catalyst mainly was linear, and thereby suggested that linear CO participated in the DMO formation [26]. However, the band of linear CO was overlapped with the gaseous CO, and it was difficult to evaluate the amount of linear and bridged CO [26].

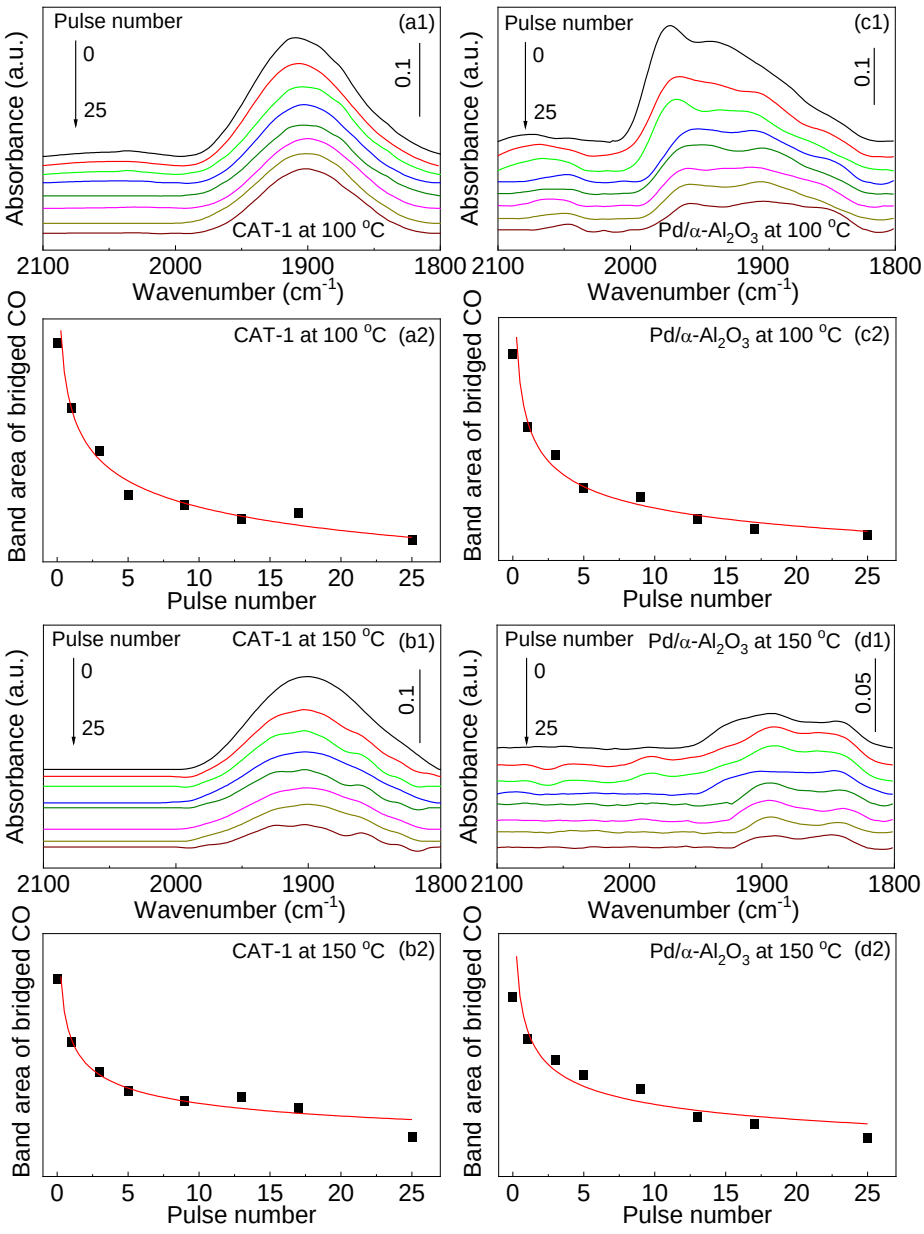

Figure 10. Dynamic changes of DRIFTS spectra on the (a,b) Pd/AlOOH/Al-fiber (CAT-1) and (c,d) Pd/α-Al_2O_3 catalysts with pre-adsorbed CO reactant at 100 ºC and 150 ºC as a function of CH_3ONO pulse number (0, 1, 3, 5, 9, 13, 17 and 25), and the relationship between the band area of bridged CO (2005−1800 cm^{-1}) and pulse number. (Reproduced with permission from ref.[29]. Copyright 2016 Elsevier).

5.2. Reaction pathway and rate-determining step

Reaction pathway analysis shows the consumption of reactants, the formation of intermediates and products during the reaction process [136,137]. Based on the stoichiometric equation of DMO formation (Eq. 10), Waller [138] proposed a possible $COOCH_3$–$COOCH_3$ coupling route. The reaction was initiated by the oxidative addition of CH_3ONO reactant to generate an intermediate NO–Pd–OCH_3, followed by the insertion of CO reactant to generate an intermediate NO–Pd–$COOCH_3$, which was coupled with another NO–Pd–$COOCH_3$ intermediate to yield DMO. The CO–$COOCH_3$ coupling route involving the consecutive CO insertion into NO–Pd–$COOCH_3$ forming NO–Pd–$COCOOCH_3$ and reacting with NO–Pd–OCH_3 to produce DMO was also proposed [138]. The reaction pathway focused on the two ways of coupling carbon atoms, including the $COOCH_3$–$COOCH_3$ and CO–$COOCH_3$ coupling routes.

The reaction mechanism was revealed by conducting a series of *in situ* DRIFTS experiments [93]. An unknown intermediate consisting of C=O and C–O stretching vibrations and CH_3 rocking vibration was captured by both steady-state and dynamic pulse experiments. The intermediate was confirmed to be $COCOOCH_3$* through the dissociative adsorption of $CH_3COCOCl$ thus matching well with the observed intermediates. Thus, the CO–$COOCH_3$ coupling route was proposed to be more

probable (Scheme 9); the consumption of $COCOOCH_3$* was the rate-determining step for the DMO formation [93].

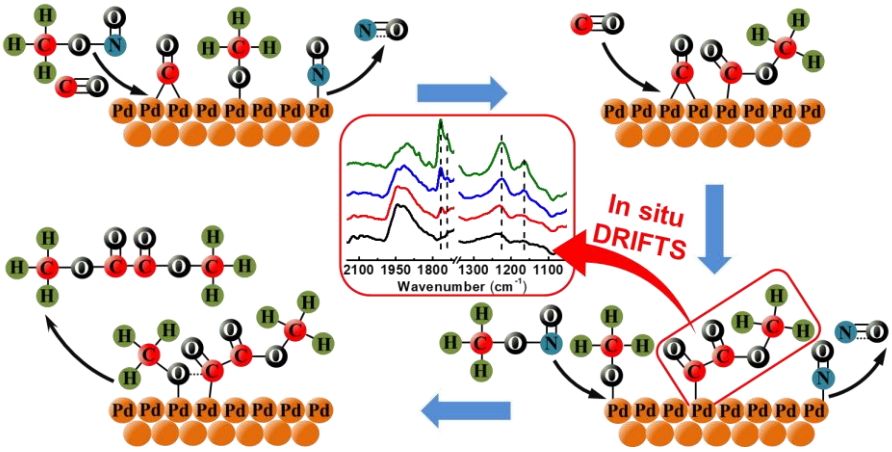

Scheme 9. Proposed mechanism of the CO oxidative coupling to DMO complied with a $CO–COOCH_3$ coupling route. (Reproduced with permission from ref.[93]. Copyright 2016 Elsevier).

The catalytic reaction mechanism on a Pd (111) surface was further elucidated by DFT [132]. The OCH_3* species was reported to approach the CO and formed the first $COOCH_3$* intermediate via a transition state (Figure 11), followed by the second $COOCH_3$* intermediate generation (an energy barrier of 15.21 kcal mol^{-1}). However, a very high energy barrier of 37.18 kcal mol^{-1} was required due to the formation of carbon-carbon bond, steric effect and electrostatic interactions. This strongly suggested that the $COOCH_3–COOCH_3$ coupling route was extremely difficult. Compared with the $COOCH_3–COOCH_3$ coupling, the $CO–COOCH_3$ coupling route occurred at early stage with a low steric hindrance, and only needed to overcome a moderate barrier of 27.39 kcal mol^{-1}. In summary, the $CO–COOCH_3$ coupling route was suggested to be more favorable than the $COOCH_3–COOCH_3$ coupling route on the Pd (111) surface [132].

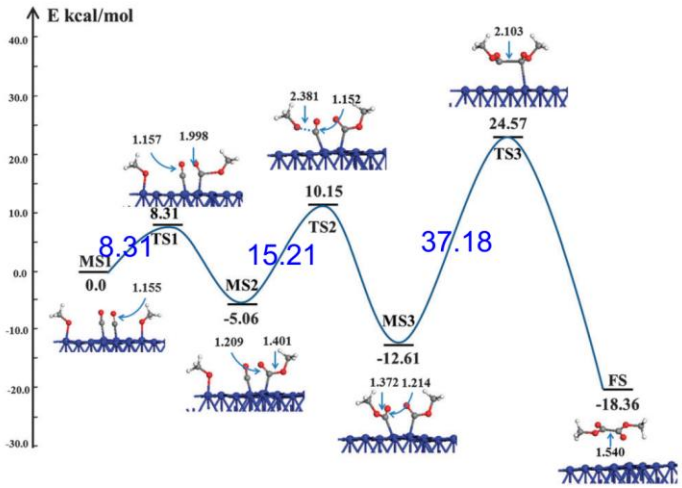

Figure 11. The energy profile of the $COOCH_3$–$COOCH_3$ coupling route for the CO oxidative coupling to DMO. All energies are given in kcal mol^{-1}. The MS and TS represent the intermediate state and transition state, respectively. (Reproduced with permission from ref.[132]. Copyright 2015 Royal Society of Chemistry).

Han et al. [139] also investigated the catalytic reaction mechanism on a Pd (111) surface by DFT. As shown in Scheme 10, three possible pathways for the CO oxidative coupling to DMO were considered, including $COOCH_3$–$COOCH_3$ (Path 1), CO–$COOCH_3$ (Path 2) and CO–CO coupling routes (Path 3). The OCH_3* approached the carbon of the adsorbed CO* through its oxygen forming the first $COOCH_3$* (Path 1, Figure 12). The formation of the second $COOCH_3$* was exothermic (–17.5 kJ mol^{-1}) with an energy barrier of 52.5 kJ mol^{-1} (Path 1, Figure 12). Subsequently, DMO was generated by two $COOCH_3$* coupling with a high energy barrier of 120.6 kJ mol^{-1}, which was the rate-determining step of Path 1. In Path 2, the formation of $COCOOCH_3$* needed to overcome a high energy barrier of 160.1 kJ mol^{-1} (Figure 12). In Path 3, the coupling of two adsorbed CO* was accompanied by a high energy barrier of 165.0 kJ mol^{-1}. As a result, the $COOCH_3$–$COOCH_3$ coupling route was suggested as the favorable pathway for the CO oxidative coupling to DMO on the Pd (111) surface

(Figure 12). This result is varying to the previous DFT calculations, possibly due to the differences in software packages (Dmol^3 software package *vs.* Vienna ab initio simulation package (VASP)) used and Pd models applied (five-layer slabs with a $p(\sqrt{3} \times \sqrt{3})$ supercell *vs*. three-layer supercell with dimensions of 3 × 4 × 1) [132]. In addition, the formation of dimethyl carbonate had to overcome a high energy barrier of 153.5 kJ mol^{-1}, which was much higher than 120.6 kJ mol^{-1} of $COOCH_3$–$COOCH_3$ coupling to DMO [139]. This was consistent with the fixed-bed result reporting the high DMO selectivity of 94% while the low selectivity of dimethyl carbonate was only 6% [29].

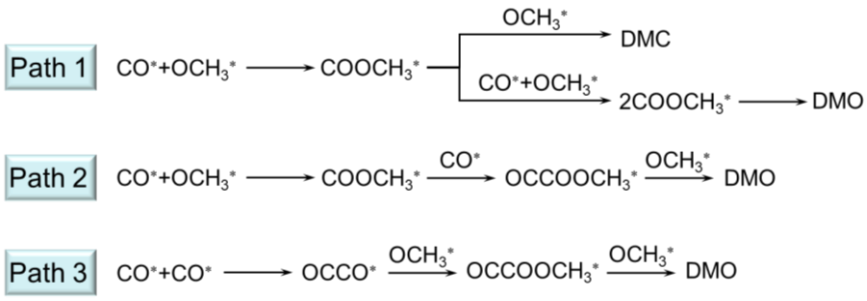

Scheme 10. The three possible pathways for the CO oxidative coupling to DMO. Reproduced with permission from ref.[139]. Copyright 2018 Royal Society of Chemistry).

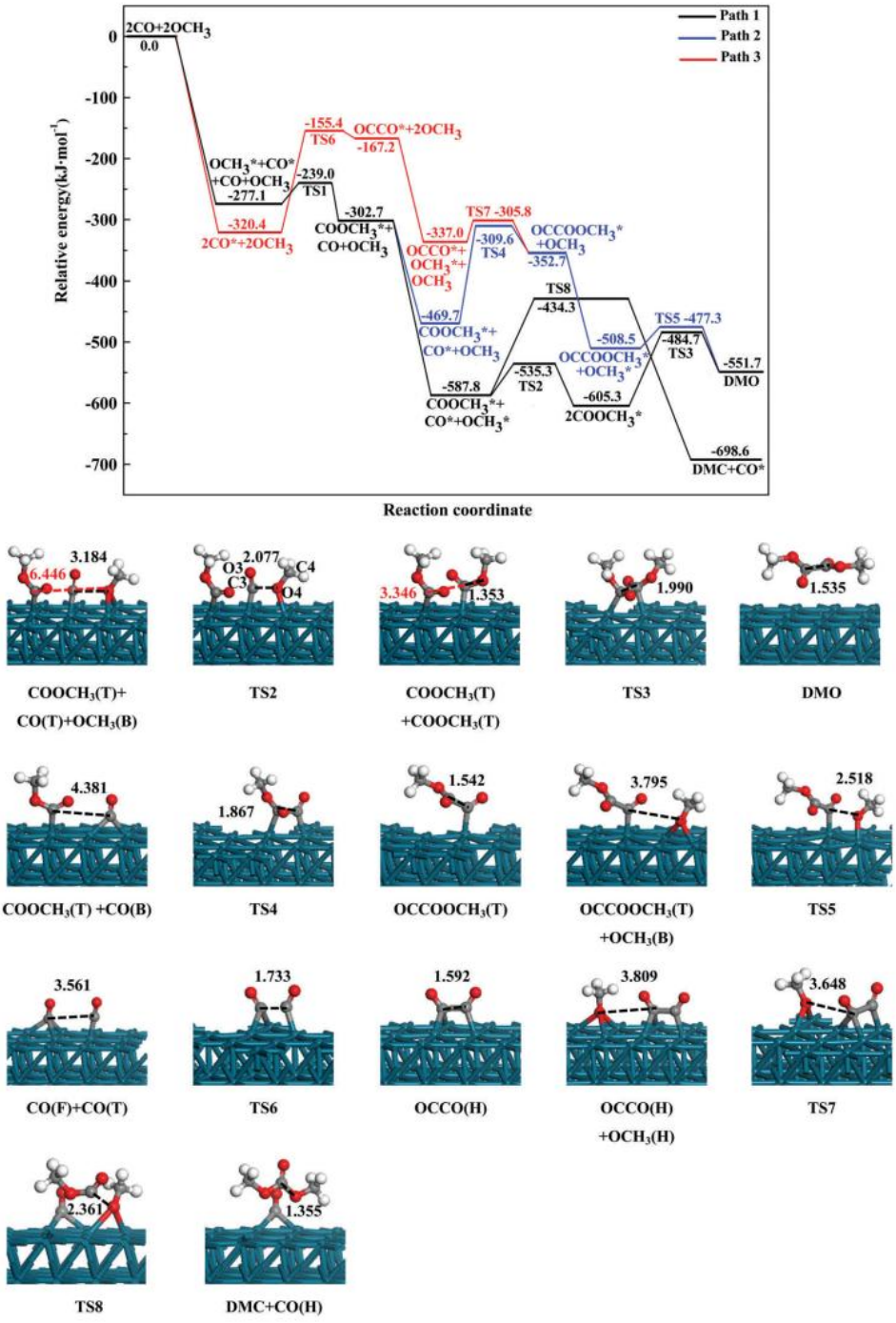

Figure 12. Potential energy diagram of the CO oxidative coupling to DMO, and the corresponding configuration of initial states, transition states and final states on the Pd (111) surface. (Reproduced with permission from ref.[139]. Copyright 2018 Royal Society of Chemistry).

A comprehensive kinetic model including the $COOCH_3$–$COOCH_3$ and CO–$COOCH_3$ coupling routes was proposed (Scheme 10) [25]. The Langmuir-Hinshelwood (LH) mechanism with dissociation of CH_3ONO based on the $COOCH_3$–$COOCH_3$ coupling described well the overall reaction. The kinetic model demonstrated that the strong competitive adsorption of CO and NO would suppress the reaction rate. The correctness of the model was verified by three pilot-scale fixed-bed reactors. The kinetic model is an essential basis for the design of commercial reactor and optimization of operation conditions.

5.3. Reaction kinetics

Reaction kinetics study provides the important information about reaction rates, reaction intermediates and pathways [140]. Several features of the CO oxidative coupling to DMO have been observed by Uchiumi et al. [38]: (1) the formation rate of DMO reached a maximum when the partial pressure of CO reactant was about 20%; (2) the reaction rate depended on the partial pressure of CH_3ONO reactant; (3) the NO product could retard the DMO formation; and (4) the reaction rate was independent of the concentration of alcohol. A power-law equation according to a Langmuir-Hinshelwood mechanism was also reported (Eq. 15) [93]. The reaction order of 0.83 with respect to CH_3ONO reactant indicated the reaction rate was related to the partial pressure of CH_3ONO. The reaction order of −1.11 of CO reactant showed a suppression effect on the reaction rate, suggesting the competitive adsorption between CO and CH_3ONO reactants on the active sites.

$$-r_{CO} = 4.3 \times 10^7 \, exp\left(-\frac{9.40 \times 10^4}{RT}\right) P_{CO}^{-1.11} P_{MN}^{0.83} \qquad (15)$$

Meng et al. [141,142] studied the reaction kinetics of the CO oxidative coupling to diethyl oxalate ($2CH_3CH_2ONO + 2CO \rightarrow (COOCH_2CH_3)_2 + 2NO$), similar to the CO

oxidative coupling to DMO ($2CH_3ONO + 2CO \rightarrow (COOCH_3)_2 + 2NO$). First, both internal and external diffusion by kinetic experiments were studied. The reaction was found to be kinetically controlled at the following conditions: a catalyst particle size less than 3 mm, a flow rate larger than 0.1 mol h^{-1} and a reaction temperature below 116 ºC. The power-law model was proposed and kinetic parameters were calculated according to the damped least-square method (Eqs. 16 and 17). The generated nitrogen monoxide partially occupied the active sites and thus showed an inhibiting effect of the formation of diethyl oxalate.

$$r_{DEO} = 234\ exp\left(-\frac{1.87 \times 10^4}{RT}\right) P_{CO}^{1.03} P_{EN}^{0.76} P_{NO}^{-0.81} \quad (16)$$

$$r_{DEC} = 4.68\ exp\left(-\frac{1.79 \times 10^4}{RT}\right) P_{CO}^{0.88} P_{EN}^{0.93} P_{NO}^{-0.35} \quad (17)$$

Where *DEO* is diethyl oxalate, *DEC* diethyl carbonate, and *EN* ethyl nitrite.

Further microkinetic modeling of surface reactions allowing better understanding of the reaction mechanism was reported [143,144]. The microkinetic analysis with DFT was used to identify the key reaction intermediates and rate-determining step, thereby providing critical information for catalysts design [145-149]. The microkinetic modeling provided information of catalytic activity and selectivity for the CO oxidative coupling to DMO on Pd (111), Pd-Cu (111) and Pd-Al (111) surfaces [139,150]. All possible reaction steps for DMO formation were listed in Table 2. The site balance of surface coverage (θ) of different reaction intermediates and active sites (*) can be presented as follows (Eq. 18).

$$\theta_{CO} + \theta_{OCH_3} + \theta_{COOCH_3} + \theta_{OCCOOCH_3} + \theta_{OCCO} + \theta^* = 1 \quad (18)$$

Table 2 All possible elementary reactions of the DMO formation for the CO oxidative coupling to DMO. (Reproduced with permission from ref.[139]. Copyright 2018 Royal Society of Chemistry).

No.	Rate constant	Elementary reactions (*, a surface site)
1	k_1	$CO^* + OCH_3^* \rightarrow COOCH_3^*$
2	k_2	$COOCH_3^* + CO^* + OCH_3^* \rightarrow 2COOCH_3^* + *$
3	k_3	$2COOCH_3^* \rightarrow (COOCH_3)_2 + 2*$
4	k_4	$COOCH_3^* + CO^* \rightarrow OCCOOCH_3^* + *$
5	k_5	$OCCOOCH_3^* + OCH_3^* \rightarrow (COOCH_3)_2 + 2*$
6	k_6	$2CO^* \rightarrow OCCO^* + *$
7	k_7	$OCCO^* + OCH_3^* \rightarrow OCCOOCH_3^* + *$
8	k_8	$COOCH_3^* + OCH_3^* \rightarrow CO(OCH_3)_2 + 2*$

The calculated rate constants (k) (Table 3) indicated that the elementary reactions of $2COOCH_3^* \rightarrow (COOCH_3)_2 + 2*$, $COOCH_3^* + CO^* \rightarrow OCCOOCH_3^* + *$, and $2CO^* \rightarrow OCCO^* + *$, were the rate-determining steps in the Path 1, Path 2 and Path 3 of DMO formation (Scheme 10) on Pd (111) surface, respectively [139]. The surface coverage (θ) of $COOCH_3^*$ was about 1.00 while the sum of other reaction intermediates was lower than 0.01. Based on the law of mass action, the reaction rates (r) of DMO and DMC were proportional to the surface coverage (θ) of reaction intermediates and rate constants (k). The calculated reaction rates of DMO (r_{DMO}) were much higher than that of DMC in the temperature range of 102–142 ºC (e.g., r_{DMO} of 4.72×10^{-6} s^{-1} *vs.* r_{DMC} of 4.02×10^{-14} s^{-1} at 102 ºC; Table 3) [139]. This suggested that the formation of DMC byproduct was difficult, which was consistent with experimental

results (DMO selectivity of 98% *vs.* DMC selectivity of 2% at 110 ºC on the Pd-based catalysts) [29].

Table 3 The rate constant (k, s^{-1}), surface coverage (θ) of different reaction intermediates, and reaction rates (r, s^{-1}) of DMO and DMC in the temperature range of 102–142 ºC on Pd (111) surface for the CO oxidative coupling to DMO. (Reproduced with permission from ref.[139]. Copyright 2018 Royal Society of Chemistry).

Entry	102 ºC	112 ºC	122 ºC	132 ºC	142 ºC
k_1	2.13×10^{6}	2.93×10^{6}	3.97×10^{6}	4.59×10^{6}	6.94×10^{6}
k_2	2.52×10^{4}	3.89×10^{4}	5.87×10^{4}	7.16×10^{4}	1.26×10^{5}
k_3	4.72×10^{-6}	1.29×10^{-5}	3.35×10^{-5}	5.31×10^{-5}	1.98×10^{-4}
k_4	1.54×10^{-10}	5.92×10^{-10}	2.12×10^{-9}	3.92×10^{-9}	2.27×10^{-8}
k_5	4.03×10^{8}	5.28×10^{8}	6.81×10^{8}	7.70×10^{8}	1.09×10^{9}
k_6	2.94×10^{-11}	1.17×10^{-10}	4.32×10^{-10}	8.12×10^{-10}	4.91×10^{-9}
k_7	1.49×10^{9}	1.98×10^{9}	2.60×10^{9}	2.96×10^{9}	4.30×10^{9}
k_8	1.43×10^{-9}	5.23×10^{-9}	1.79×10^{-8}	5.79×10^{-8}	1.77×10^{-7}
$\theta*$	5.04×10^{-27}	1.83×10^{-26}	7.60×10^{-26}	2.53×10^{-25}	1.07×10^{-24}
θ_{CO}	7.76×10^{-8}	9.27×10^{-8}	1.35×10^{-7}	1.64×10^{-7}	2.68×10^{-7}
θ_{OCH3}	2.81×10^{-5}	4.68×10^{-5}	6.20×10^{-5}	6.94×10^{-5}	1.04×10^{-4}
θ_{COOCH3}	1.00	1.00	1.00	1.00	1.00
$\theta_{COCOOCH3}$	1.06×10^{-21}	2.22×10^{-21}	6.76×10^{-21}	1.21×10^{-20}	5.33×10^{-20}
θ_{OCCO}	4.22×10^{-30}	1.08×10^{-29}	4.86×10^{-29}	1.07×10^{-28}	7.88×10^{-28}
r_{DMO}	4.72×10^{-6}	1.29×10^{-5}	3.35×10^{-5}	5.31×10^{-5}	1.98×10^{-4}
r_{DMO}	4.02×10^{-14}	2.45×10^{-13}	1.11×10^{-12}	4.02×10^{-12}	6.04×10^{-12}

6. CO oxidative coupling to dimethyl oxalate: process intensification using structured catalysts

For commercial applications, powder catalysts need to be shaped and meet the requirements for industrial reactors [151,152]. The packed-bed/fixed-bed reactors are widely used for catalytic processes. However, the random nature of the shaped catalyst packing poses some problems, such as flow maldistributions, dead zones, bed channeling, packing issues and high pressure drop [153]. Additionally, unexpected hot spots and thermal runaway may occur for strong exothermic reactions [154]. These negative effects result in poor intraparticle/interbed mass and heat transfer rates, and thus decrease the overall performance [155].

To address the problems of traditional packed-bed reactors, structured catalysts and reactors (SCRs) have been developed. The most well-known SCRs are the ceramic honeycomb type catalysts [156]. The honeycomb catalysts consist of millimeter-sized opening parallel channels with a void fraction of 0.7–0.9 (lower than 0.5 for typical packed-bed reactors). Such structures of SCRs showed a pressure drop up to two orders of magnitude lower than that in conventional packed-bed reactors [157]. The SCRs showed remarkable enhancement and improvement in both catalytic performance and reactor engineering [158,159]. The SCRs allowed a controlled integration of active components with optimized compositions and morphologies [160,161]. Thus the SCRs were used in hydrogenation of dimethyl oxalate [162], dehydrogenation of ethane [163], methane reforming to syngas [164], catalytic combustion of methane [165], and methanol to propylene processes [166]. The SCRs demonstrated enhanced heat/mass transfer, low pressure drop, uniform flow patterns and residence times [167,168]. More efficient reactor design and operation were achieved for decoupling of hydrodynamics and reaction kinetics [169,170].

6.1. CO oxidative coupling to dimethyl oxalate: heat transfer

Studies into heat transfer in a fixed-bed reactor has been a hot topic. The hot spot generation (sudden and uncontrollable temperature increase) at the catalyst bed typically occurred in the highly exothermic reactions [171]. The CO oxidative coupling to DMO is a strong exothermic reaction with a $\Delta H_{25\ ^{\circ}C}$ of −159 kJ mol^{-1} (Eq. 19) [29]. Beyond thermal runaway risks, poor control of the bed temperature causes the catalysts deactivation, sintering and undesired side reactions [172]. As previously stated, most studies were focused on the catalysts in the CO oxidative coupling to DMO process. However, less attention was paid to the heat properties of the CO oxidative coupling to DMO, including the hot spot and the thermal runaway. The reaction temperature, gas hourly space velocity (GHSV), reactant concentration of CO and methyl nitrite should be strictly controlled in order to decrease the hot-spot temperature in the scale-up production of DMO. Usually, a tubular fixed-bed reactor must be used to enhance the heat transfer in the CO oxidative coupling to DMO (Figure 13) [173]. In fact, the tubular fixed-bed reactor has a low capacity of less than 50,000 tons per year; This means if the plant has a total capacity of 200,000 tons per year, the four tubular fixed-bed reactors should be used in parallel. To increase the reactor capacity, a two-dimensional heterogeneous reactor model was established to simulate and optimize the tubular fixed-bed reactor. After the operating conditions of the reactors were optimized by the genetic algorithm, the annual production capacity could be increased to 120,000 tons per reactor [174].

$$2CH_3ONO + 2CO \rightarrow (COOCH_3)_2 + 2NO \qquad \Delta H_{25\ ^{\circ}C} = -159\ kJ\ mol^{-1} \qquad (19)$$

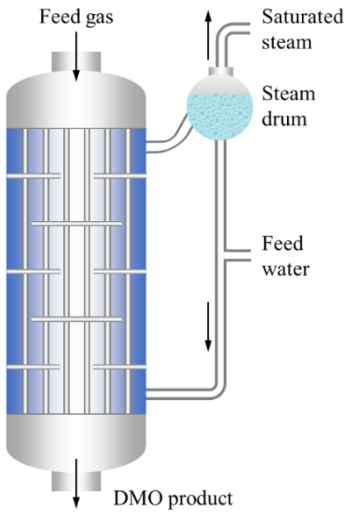

Figure 13. Diagram of an industrial tubular fixed-bed reactor for the CO oxidative coupling to DMO.

A model of one-dimensional pseudo-homogeneous reactor was established based on the kinetic data obtained from CO oxidative coupling to DMO in a tubular fixed-bed reactor [175]. The sensitivity of hot-spot temperature was studied with the one-dimensional pseudo-homogeneous model (Figure 14). The results suggested that the coolant temperature had a significant impact on the hot-spot temperature (Figure 14). The gas hourly space velocity less than 2000 h^{-1} led to a thermal runaway in the reactor. In addition, a two-dimensional pseudo-homogeneous reactor model was built to simulate the performance of fixed-bed reactor for CO coupling to diethyl oxalate [176]. The validity of the reactor model was confirmed by comparing the model prediction and the measured data from different-scale processes. The simulated results showed that the coolant temperature had a remarkable effect on the reactor bed temperature and the hot spot in the reactor. In practice, the high coolant temperature resulted in an increase of reactor temperature. Thus, increased temperature of the reactor would accelerate reaction rates and accumulate the heat. As a consequence, this further would lead to an increase of hot spot temperature and backward shift of hot spot position [177]. The order

of parameter affecting the hot spot temperature was as follow: coolant temperature > feed gas temperature > carbon monoxide composition > space velocity (Figure 15).

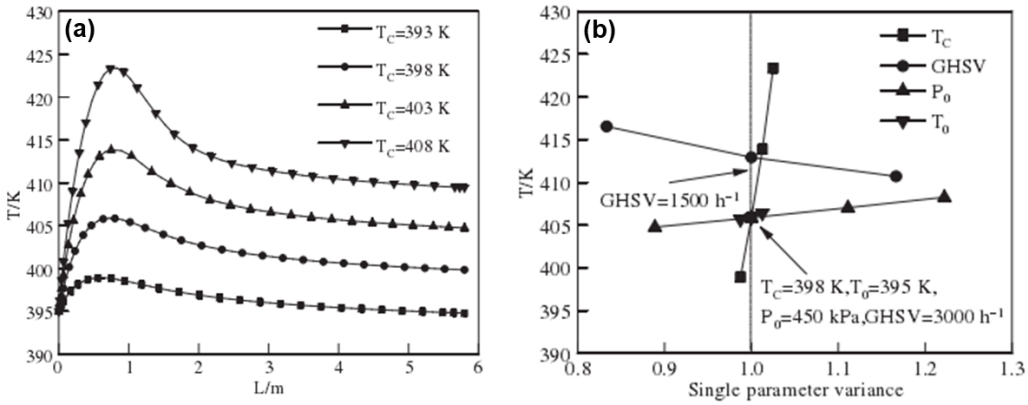

Figure 14. (a) Effect of coolant temperature (T_C) on the axial temperature' distribution; (b) effect of the T_C, gas hourly space velocity (GHSV), inlet pressure (P_0) and inlet temperature (T_0) on the hot-spot temperature. (Reproduced with permission from ref.[174]. Copyright 2022 Chemical Industry Press (China)).

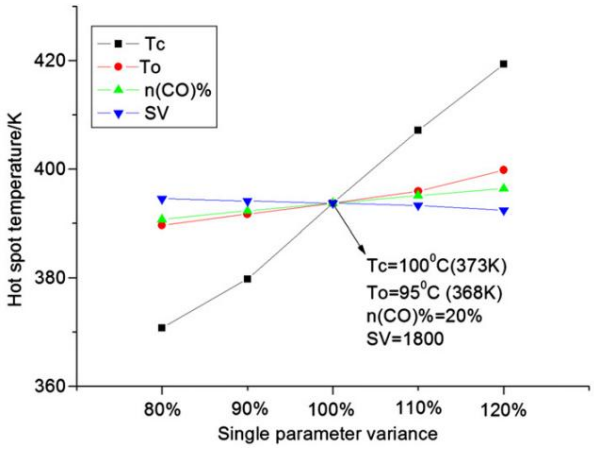

Figure 15. Effects of the coolant temperature (T_C), feed gas temperature (T_0), carbon monoxide composition (n_{CO}) and space velocity (SV) on the hot-spot temperature. (Reproduced with permission from ref.[177]. Copyright 2011 Elsevier).

Moreover, the effects of reactor temperature jump on the deactivation of a Pd-Fe/α-Al_2O_3 catalyst for CO oxidative coupling to diethyl oxalate were investigated [178]. The degree of catalyst deactivation was closely related to the position of the catalyst in the reactor. After the destructive catalyst test at a high temperature, the size of Pd particle was increased substantially. After the deactivation, most of Pd^0 species were oxidized to Pd^{2+} and Fe^{2+} species to Fe^{3+}. The deactivated catalyst could be partially regenerated, but the catalytic activity of regenerated catalyst was lower than the fresh catalyst.

6.2. CO oxidative coupling to dimethyl oxalate: preparation of structured catalysts

The preparation of structured catalysts is considered as a promising strategy to address the weaknesses of traditional fixed-bed reactors thanks to the enhanced hydrodynamics and improved heat/mass transfer [179]. The structured supports mainly include ceramic (cordierite, SiC and Al_2O_3) and metal (aluminum, copper, stainless steel and FeCrAl) substrates in the shape of honeycomb monoliths, foams and fibers [157,180]. The preparation of structured catalysts involved a surface pre-treatment of substrates, followed by activation [155,169,170]. The approaches applied for structured catalysts are shown in Figure 16 [155].

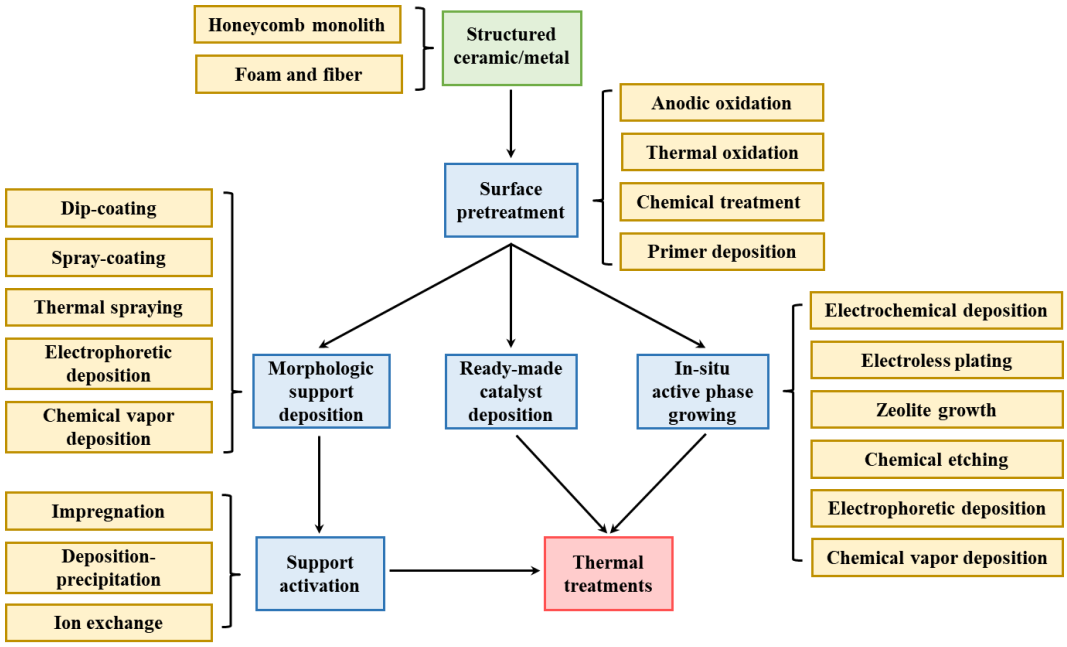

Figure 16. Main approaches for the preparation of structured catalysts. (Reproduced with permission from ref.[155]. Copyright 2014 Royal Society of Chemistry).

Since the CO oxidative coupling to DMO is a strong exothermic reaction with a $\Delta H_{25\,^{\circ}C}$ of −159 kJ mol^{-1} (Eq. 19), the cordierite monolith was used to enhance the heat and mass transfer. A Pd-Fe/α-Al_2O_3/cordierite monolithic catalyst was prepared by a dip-coating process followed by the active phase impregnation (Figure 17) [80,81]. The Pd-Fe/α-Al_2O_3/cordierite monolithic catalyst was tested in the CO coupling to DMO and it was found that their catalytic performance was dependent on the particle size of α-Al_2O_3 sol, thickness of α-Al_2O_3 coating, pore structure and acidity of α-Al_2O_3, and distribution of active metals. The monolithic catalyst exhibited a much higher Pd efficiency of 733 DMO(g) $Pd(g)^{-1}$ h^{-1} than a reference Pd-Fe/α-Al_2O_3 granular catalyst of 60 DMO(g) $Pd(g)^{-1}$ h^{-1}. The high activity was attributed to the honeycomb structure and the large pore size of α-Al_2O_3 coating [80].

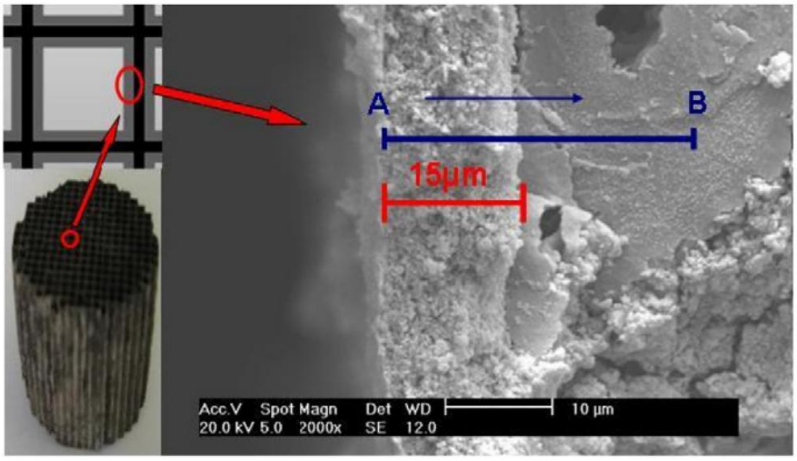

Figure 17. Photograph and SEM image of cross-section of the Pd-Fe/α-Al_2O_3/cordierite monolithic catalyst with an α-Al_2O_3 coating of about 15 μm. (Reproduced with permission from ref.[81]. Copyright 2011 Elsevier).

The microfibrous-structured Al-fiber felt with an open three-dimensional porous network was used for the CO coupling to DMO [29]. As shown in Figure 18, the pristine Al-fiber felt has an inactive surface and low surface area. After a water-only hydrothermal oxidation ($2Al + 4H_2O \rightarrow 2AlOOH + 3H_2$), the free-standing boehmite (AlOOH) nanosheets were formed, and disorderedly aligned to a homogeneous honeycomb-like shell along with the Al-fiber core. The active component of palladium was highly dispersed on the AlOOH nanosheets. The as-obtained Pd/AlOOH/Al-fiber catalyst exhibited two times higher intrinsic activity (i.e., turnover frequency) than the Pd/α-Al_2O_3 reference catalyst. The Pd-hydroxyl synergistic interactions were responsible for the enhanced catalytic performance as discussed above [29]. The effect of morphology of AlOOH nanosheets [82,94], phase of AlOOH [84], promoter of carbon [83], loading method of Pd [85] and catalytic reaction mechanism [93] on the Pd/AlOOH/Al-fiber catalyst were investigated.

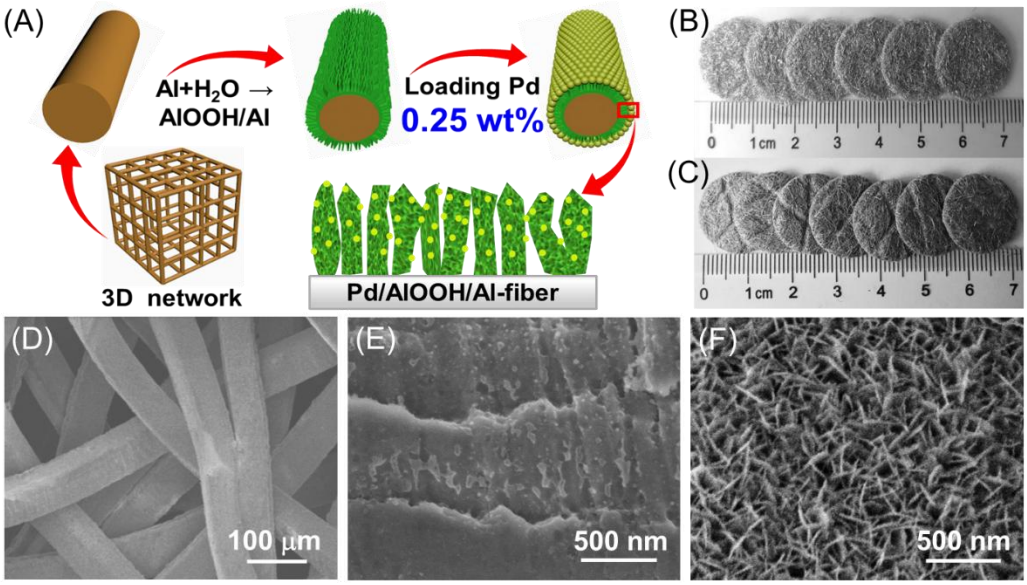

Figure 18. (A) Strategy for preparation of Pd/AlOOH/Al-fiber catalyst. Optical photographs of (B) pristine Al-fiber felt and (C) AlOOH/Al-fiber. SEM images of (D,E) pristine Al-fibers and (F) Pd/AlOOH/Al-fiber catalyst. (Reproduced with permission from ref.[82]. Copyright 2017 American Chemical Society).

To examine the ability for heat-transfer, the computational fluid dynamics (CFD) simulation was employed. The temperature distribution in the microfibrous-structured catalyst (Pd/α-Al_2O_3/Al-fiber) and randomly packed catalyst (Pd/α-Al_2O_3) was obtained. As shown in Figure 19, the simulated temperature distribution of the microfibrous-structured Pd/α-Al_2O_3/Al-fiber catalyst was more homogeneous than the Pd/α-Al_2O_3 catalyst; the former exhibited a hot spot with temperature rise of 8 ºC, while the latter had a temperature rise of 30 ºC [84]. The lower temperature rise was assigned to the enhanced thermal conductivity of microfibrous-structured Al-fiber, which rapidly dissipated the reaction heat. The experimental results were consistent with the CFD result. The temperature rise measured by a K-type thermocouple was 5 ºC on the Pd/α-Al_2O_3/Al-fiber catalyst, and 11 ºC on the Pd/α-Al_2O_3 catalyst [84].

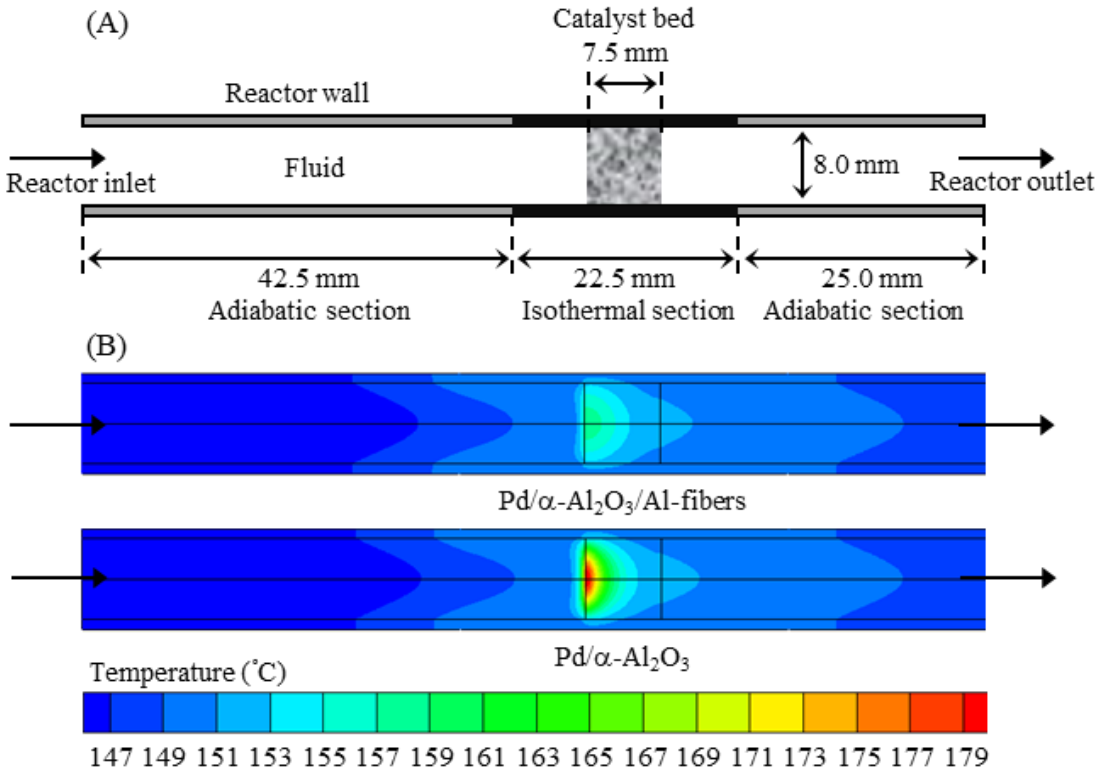

Figure 19. (A) Schematic diagram of the tubular reactor with one isothermal section and two adiabatic sections for CFD simulation, and (B) reactor temperature distribution obtained by the steady-state CFD simulation on the Pd/α-Al_2O_3/Al-fiber catalyst and the Pd/α-Al_2O_3 reference catalyst. (Reproduced with permission from ref.[84]. Copyright 2020 Elsevier).

7. Summary and perspective

We have witnessed the remarkable progress and applications of coal to ethylene glycol (EG) via DMO hydrogeneration during the past fourteen years. The world's first plant was built in 2009 in China, and as of 2023 there are more than 30 plants running with total capacity of about 7.0 million tons. However, there are still challenges that have to be addressed in the near future. The applications of DMO should not be limited to the production of EG. Potentially the consumption of DMO to high-value chemicals, such as methyl glycolate, diphenyl carbonate and dimethyl carbonate have to be facilitated.

Moreover, the emerging synthesis of EG through non-DMO routes, such as photocatalysis (formaldehyde to EG, methanol to EG and methane to EG) and electrocatalysis (CO_2 to EG, CO_2 to EG and ethylene to EG) has attracted significant attention due to the moderate conditions applied. The coal to EG process is relatively mature, while the emerging technological routes still face numerous challenges in large-scale production.

More attention has been paid to the development of high-performance catalyst for the CO oxidative coupling to DMO. The effects of the active component (Pd), catalyst supports and promoters have been widely investigated. Reducing the amount of the Pd precious metal and development of non-noble metal catalysts are of great importance and are under intensive fundamental and industrial-related studies. The rapid development of computational chemistry, particularly DFT, provides the potential ideas of new catalysts design. The DFT indicated that the Cu monolayer supported on the carbon-terminated $Mo_2C(001)$ ($Cu_{ML}/Mo_2C(001)$-C) exhibited excellent catalytic activity, making it a potential candidate to replace the noble metal Pd catalyst.

Significant attention was paid to understanding the mechanism of DMO synthesis. The two possible reaction mechanisms were proposed, including the intramolecular coupling and the double carbonylation. The reaction species of CO*, OCH_3*, $COOCH_3$*, $COCOOCH_3$* and NO* were found to be involved. The rate determining step is the formation of $COCOOCH_3$* ($CO^* + COOCH_3^* \rightarrow COCOOCH_3^* + *$) for the double carbonylation pathway, while is the coupling of two $COOCH_3$* for the intramolecular coupling pathway ($COOCH_3^* + COOCH_3^* \rightarrow (COOCH_3)_2^* + *$). Based on the proposed reaction mechanism, various catalyst models such as Pd-doped Cu (111) and Pd_{ML}/Ni (111) were studied theoretically in order to reduce the use of Pd precious metal.

The low efficiency of the current industrial-scale reactor is caused by the safety concern due to the exothermic feature of CO oxidative coupling to DMO. Structured catalysts (metal foams and fibers) pave the way to the "ideal" reactor demonstrating ultralow pressure drop and remarkable decrease of hot-spot temperature. Both Pd-Fe/α-Al_2O_3/cordierite monolithic and microfibrous-structured Pd/Al-fiber catalysts not only delivered the satisfactory activity and stability for DMO synthesis, but also showed the intensified heat and mass transfer of the unique structures. However, to date, structured catalysts have not been commercially utilized in the DMO synthesis. They may face challenges associated with high cost and complex manufacturing processes. Additionally, further optimization of mass and heat transfer behaviour has to be considered prior their application on an industrial scale.

Declaration of Competing Interest

The authors declare no competing financial interest.

Acknowledgements

This project was financially supported by the National Key R&D Program of China (2022YFE0116000), National Natural Science Foundation of China (21908246, 21975285 and 22175200), Key Research and Development Program (Major Scientific and Technological Innovation Project) of Shandong Province (2021ZLGX06) and Sino-French International Research Network (IRN) "Zeolites".

References

[1] Zimmerman, J. B.; Anastas, P. T.; Erythropel, H. C.; Leitner, W. Designing for a Green Chemistry Future. *Science*. 2020, *367*(6476), 397–400. DOI: 10.1126/science.aay3060.

[2] Sheldon, R. A. Green Chemistry: Principles and Case Studies. *Angew. Chem. Int. Ed.* 2021, *60*(2), 538–539. DOI: 10.1002/anie.202008458.

[3] He, M.; Sun, Y.; Han, B. Green Carbon Science: Scientific Basis for Integrating Carbon Resource Processing, Utilization, and Recycling. *Angew. Chem. Int. Ed.* 2013, *52*(37), 9620–9633. DOI: 10.1002/anie.201209384.

[4] Bedard, J.; Chiang, H.; Bhan, A. Kinetics and Mechanism of Acetic Acid Esterification with Ethanol on Zeolites. *J. Catal.* 2012, *290*, 210–219. DOI: 10.1016/j.jcat.2012.03.020.

[5] Yadav, G. D.; Mehta, P. H. Heterogeneous Catalysis in Esterification Reactions: Preparation of Phenethyl Acetate and Cyclohexyl Acetate by Using a Variety of Solid Acidic Catalysts. *Ind. Eng. Chem. Res.* 1994, *33*(9), 2198–2208. DOI: 10.1021/ie00033a025.

[6] Rogers, L.; Jensen, K. F. Continuous Manufacturing-the Green Chemistry Promise? *Green Chem.* 2019, *21*(13), 3481–3498. DOI: 10.1039/c9gc00773c.

[7] Jin, Z.; Wang, L.; Zuidema, E.; Mondal, K.; Zhang, M.; Zhang, J.; Wang, C.; Meng, X.; Yang, H.; Mesters, C.; Xiao, F. Hydrophobic Zeolite Modification for in Situ

Peroxide Formation in Methane Oxidation to Methanol. *Science.* 2020, *367*(6474), 193–197. DOI: 10.1126/science.aaw1108.

[8] Zhou, W.; Cheng, K.; Kang, J.; Zhou, C.; Subramanian, V.; Zhang, Q.; Wang, Y. New Horizon in C1 Chemistry: Breaking the Selectivity Limitation in Transformation of Syngas and Hydrogenation of CO_2 into Hydrocarbon Chemicals and Fuels. *Chem. Soc. Rev.* 2019, *48*(12), 3193–3228. DOI: 10.1039/C8CS00502H.

[9] Zuo, J.; Lai, Y.; Xie, Y.; Hong, B.; Ye, L.; Xu, H.; Tsang, S. C. E.; Yuan, Y. Design and Development of Heterogeneous Catalysts for Sustainable Formic Acid-Mediated Alkylation of Aromatics. *Cell Rep. Phys. Sci.* 2023, *4*(6), 101416. DOI: 10.1016/j.xcrp.2023.101416.

[10] Zhang, Q.; Yu, J.; Corma, A. Applications of Zeolites to C1 Chemistry: Recent Advances, Challenges, and Opportunities. *Adv. Mater.* 2020, *32*(44), 2002927. DOI: 10.1002/adma.202002927.

[11] Chen, G.; Waterhouse, G. I. N.; Shi, R.; Zhao, J.; Li, Z.; Wu, L. Z.; Tung, C. H.; Zhang, T. From Solar Energy to Fuels: Recent Advances in Light-Driven C1 Chemistry. *Angew. Chem. Int. Ed.* 2019, *58*(49), 17528–17551. DOI: 10.1002/anie.201814313.

[12] Chen, P.; Zhao, G.; Shi, X. R.; Zhu, J.; Ding, J.; Lu, Y. Nano-Intermetallic $InNi_3C_{0.5}$ Compound Discovered as a Superior Catalyst for CO_2 Reutilization. *iScience.* 2019, *17*, 315–324. DOI: 10.1016/j.isci.2019.07.006.

[13] Yue, H.; Ma, X.; Gong, J. An Alternative Synthetic Approach for Efficient Catalytic Conversion of Syngas to Ethanol. *Acc. Chem. Res.* 2014, *47*(5), 1483–1492. DOI: 10.1021/ar4002697.

[14] Cui, G.; Meng, X.; Zhang, X.; Wang, W.; Xu, S.; Ye, Y.; Tang, K.; Wang, W.; Zhu, J.; Wei, M.; Evans, D. G.; Duan, X. Low-Temperature Hydrogenation of Dimethyl Oxalate to Ethylene Glycol via Ternary Synergistic Catalysis of Cu and Acid-Base Sites. *Appl. Catal. B.* 2019, *248*, 394–404. DOI: 10.1016/j.apcatb.2019.02.042.

[15] Song, H.; Jin, R.; Kang, M.; Chen, J. Progress in Synthesis of Ethylene Glycol through C1 Chemical Industry Routes. *Chin. J. Catal.* 2013, *34*(6), 1035–1050. DOI: 10.1016/S1872-2067(12)60529-4.

[16] Jin, E.; Zhang, Y.; He, L.; Harris, H.; Teng, B.; Fan, M. Indirect Coal to Liquid Technologies. *Appl. Catal. A.* 2014, *476*, 158–174. DOI: 10.1016/j.apcata.2014.02.035.

[17] Cui, G.; Zhang, X.; Wang, H.; Li, Z.; Wang, W.; Yu, Q.; Zheng, L.; Wang, Y.; Zhu, J.; Wei, M. ZrO_{2-X} Modified Cu Nanocatalysts with Synergistic Catalysis towards Carbon-Oxygen Bond Hydrogenation. *Appl. Catal. B.* 2021, *280*, 119406. DOI: 10.1016/j.apcatb.2020.119406.

[18] Zhou, Z.; Li, Z.; Pan, P.; Lin, L.; Qin, Y.; Yao, Y. Progress in Technologies of Coal-Based Ethylene Glycol Synthesis. *Chem. Ind. Eng. Prog. (China)* 2010, *29*(11), 2003–2009.

[19] Zhao, Y.; Zhang, H.; Xu, Y.; Wang, S.; Xu, Y.; Wang, S.; Ma, X. Interface Tuning of Cu^{+}/Cu^{0} by Zirconia for Dimethyl Oxalate Hydrogenation to Ethylene Glycol over Cu/SiO_2 Catalyst. *J. Energy Chem.* 2020, *49*, 248–256. DOI: 10.1016/j.jechem.2020.02.038.

[20] Wang, Z.; Xu, Z.; Peng, S.; Zhou, Z.; Pan, P.; Lin, L.; Qin, Y.; Guo, G.; Yao, Y. New Catalysts for Coal to Ethylene Glycol. *Chin. J. Chem.* 2017, *35*(6), 759–768. DOI: 10.1002/cjoc.201600746.

[21] Chen, C.; Lin, L.; Ye, R.; Sun, M.; Yang, J.; Li, F.; Yao, Y. Mannitol as a Novel Dopant for Cu/SiO_2: A Low-Cost, Environmental and Highly Stable Catalyst for Dimethyl Oxalate Hydrogenation without Hydrogen Prereduction. *J. Catal.* 2020, *389*, 421−431. DOI: 10.1016/j.jcat.2020.06.008.

[22] Wang, X.; Chen, M.; Chen, X.; Lin, R.; Zhu, H.; Huang, C.; Yang, W.; Tan, Y.; Wang, S.; Du, Z.; Ding, Y. Constructing Copper-Zinc Interface for Selective Hydrogenation of Dimethyl Oxalate. *J. Catal.* 2020, *383*, 254–263. DOI: 10.1016/j.jcat.2020.01.018.

[23] Li, L.; Ren, D.; Fu, J.; Liu, Y.; Jin, F.; Huo, Z. Heterogeneous Cu_2O-Mediated Ethylene Glycol Production from Dimethyl Oxalate. *J. Energy Chem.* 2016, *25*(3), 507−511. DOI: 10.1016/j.jechem.2016.02.002.

[24] Yue, H.; Zhao, Y.; Ma, X.; Gong, J. Ethylene Glycol: Properties, Synthesis, and Applications. *Chem. Soc. Rev.* 2012, *41*(11), 4218–4244. DOI: 10.1039/C2CS15359A.

[25] Chi, Z.; Yang, L.; Li, X.; He, Y.; Xiao, W. CO Oxidative Coupling with Nitrite to Oxalate over Palladium Catalyst: A Comprehensive Kinetic Modeling. *Chem. Eng. J.* 2022, *446*. 136656. DOI: 10.1016/j.cej.2022.136656.

[26] Xu, Z.; Sun, J.; Lin, C.; Jiang, X.; Chen, Q.; Peng, S.; Wang, M.; Guo, G. High-Performance and Long-Lived Pd Nanocatalyst Directed by Shape Effect for CO Oxidative Coupling to Dimethyl Oxalate. *ACS Catal.* 2013, *3*(2), 118−122. DOI: 10.1021/cs300759h.

[27] Zhao, J.; Han, M.; Wang, Z.; Ling, L.; Zhang, R.; Wang, B. The Regulating Effect of Doping Cu on the Catalytic Performance of CO Oxidative Coupling to DMO on Pd_xCu_y/GDY: A DFT Study. *Green Energy Environ.* 2022, *7*(4), 742−754. DOI: 10.1016/j.gee.2020.11.011.

[28] Zheng, J.; Huang, L.; Cui, C.; Chen, Z.; Liu, X.; Duan, X.; Cao, X.; Yang, T.; Zhu, H.; Shi, K.; Du, P.; Ying, S.; Zhu, C.; Yao, Y.; Guo, G.; Yuan, Y.; Xie, S.; Zheng, L. Ambient-Pressure Synthesis of Ethylene Glycol Catalyzed by C_{60}-Buffered Cu/SiO_2. *Science*. 2022, *376*(6590), 288−292. DOI: 10.1126/science.abm9257.

[29] Wang, C.; Han, L.; Chen, P.; Zhao, G.; Liu, Y.; Lu, Y. High-Performance, Low Pd-Loading Microfibrous-Structured Al-Fiber@ns-AlOOH@Pd Catalyst for CO Coupling to Dimethyl Oxalate. *J. Catal.* 2016, *337*, 145−156. DOI: 10.1016/j.jcat.2016.02.008.

[30] Ye, R.; Lin, L.; Wang, L.; Ding, D.; Zhou, Z.; Pan, P.; Xu, Z.; Liu, J.; Adidharma, H.; Radosz, M.; Fan, M.; Yao, Y. Perspectives on the Active Sites and Catalyst Design for the Hydrogenation of Dimethyl Oxalate. *ACS Catal.* 2020, *10*(8), 4465−4490. DOI: 10.1021/acscatal.9b05477.

[31] Qiao, J. New Progress and Outlook Analysis on Technology, Market and Commercialization of Ethylene Glycol. *Mod. Chem. Ind. (China)* 2020, *40*(3), 11−15. DOI: 10.16606/j.cnki.issn0253-4320.2020.03.003.

[32] Peng, S.; Xu, Z.; Chen, Q.; Chen, Y.; Sun, J.; Wang, Z.; Wang, M.; Guo, G. An Ultra-Low Pd Loading Nanocatalyst with High Activity and Stability for CO Oxidative Coupling to Dimethyl Oxalate. *Chem. Commun.* 2013, *49*(51), 5707−5806. DOI: 10.1039/c3cc00219e.

[33] Dong, K.; Elangovan, S.; Sang, R.; Spannenberg, A.; Jackstell, R.; Junge, K.; Li, Y.; Beller, M. Selective Catalytic Two-Step Process for Ethylene Glycol from

Carbon Monoxide. *Nat. Commun.* 2016, *7*(1), 12075. DOI: 10.1038/ncomms12075.

[34] Sun, Y. L.; Chai, G. L. Direct Synthesis of Ethylene Glycol from Syngas. *Chemistryselect.* 2022, *7*(6),. DOI: 10.1002/slct.202103642.

[35] Ye, R.; Huang, Y. Y.; Chen, C. C.; Yao, Y. G.; Fan, M.; Zhou, Z. Emerging Catalysts for the Ambient Synthesis of Ethylene Glycol from CO_2 and its Derivatives. *Chemcomm.* 2023, *59*(19), 2711–2725. DOI: 10.1039/d2cc06313a.

[36] Wang, Z.; Sun, J.; Xu, Z.; Guo, G. CO Direct Esterification to Dimethyl Oxalate and Dimethyl Carbonate: The Key Functional Motifs for Catalytic Selectivity. *Nanoscale.* 2020, *12*, 20131–20140. DOI: 10.1039/D0NR03008B.

[37] Yamamoto, Y. Vapor Phase Carbonylation Reactions Using Methyl Nitrite over Pd Catalysts. *Catal. Surv. Asia.* 2010, *14*(3–4), 103–110. DOI: 10.1007/s10563-010-9102-8.

[38] Uchiumi, S.; Ataka, K.; Matsuzaki, T. Oxidative Reactions by a Palladium-Alkyl Nitrite System. *J. Organomet. Chem.* 1999, *576*(1–2), 279–289. DOI: 10.1016/S0022-328X(98)01064-X.

[39] Yin, A.; Guo, X.; Dai, W.; Fan, K. High Activity and Selectivity of Ag/SiO_2 Catalyst for Hydrogenation of Dimethyl Oxalate. *Chem. Commun.* 2010, *46*(24), 4348–4350. DOI: 10.1039/C0CC00581A.

[40] Gong, J.; Yue, H.; Zhao, Y.; Zhao, S.; Zhao, L.; Lv, J.; Wang, S.; Ma, X. Synthesis of Ethanol via Syngas on Cu/SiO_2 Catalysts with Balanced Cu^0-Cu^+ Sites. *J. Am. Chem. Soc.* 2012, *134*(34), 13922–13925. DOI: 10.1021/ja3034153.

[41] Zhu, Y.; Zhu, Y.; Ding, G.; Zhu, S.; Zheng, H.; Li, Y. Highly Selective Synthesis of Ethylene Glycol and Ethanol via Hydrogenation of Dimethyl Oxalate on Cu Catalysts: Influence of Support. *Appl. Catal. A.* 2013, *468*, 296–304. DOI: 10.1016/j.apcata.2013.09.019.

[42] Wang, Q.; Li, C.; Guo, M.; Luo, S.; Hu, C. Transesterification of Dimethyl Carbonate with Phenol to Diphenyl Carbonate over Hexagonal $Mg(OH)_2$ Nanoflakes. *Inorg. Chem. Front.* 2015, *2*(1), 47–54. DOI: 10.1039/C4QI00113C.

[43] Zhang, F.; Yu, X.; Ma, F.; Yang, X.; Hu, J.; Deng, Z.; Wang, G. Transesterification of Dimethyl Oxalate with Phenol over a MoO_3/SiO_2 Catalyst Prepared by Thermal Spreading. *Chin. J. Catal.* 2014, *35*(7), 1043–1053. DOI: 10.1016/S1872-2067(14)60042-5.

[44] Wang, S.; Shi, Y.; Ma, X. Microwave Synthesis, Characterization and Transesterification Activities of Ti-MCM-41. *Microporous Mesoporous Mater.* 2012, *156*, 22–28. DOI: 10.1016/j.micromeso.2012.02.011.

[45] Yuan, X.; Zhang, M.; Chen, X.; An, N.; Liu, G.; Liu, Y.; Zhang, W.; Yan, W.; Jia, M. Transesterification of Dimethyl Oxalate with Phenol over Nitrogen-Doped Nanoporous Carbon Materials. *Appl. Catal. A.* 2012, *439–440*, 149–155. DOI: 10.1016/j.apcata.2012.06.052.

[46] Kotbagi, T.; Nguyen, D. L.; Lancelot, C.; Lamonier, C.; Thavornprasert, K.; Wenli, Z.; Capron, M.; Jalowiecki-Duhamel, L.; Umbarkar, S.; Dongare, M.; Dumeignil, F. Transesterification of Diethyl Oxalate with Phenol over Sol-Gel MoO_3/TiO_2 Catalysts. *ChemSusChem.* 2012, *5*(8), 1467–1473. DOI: 10.1002/cssc.201100802.

[47] Shi, Y.; Wang, S.; Ma, X. Microwave Preparation of Ti-Containing Mesoporous Materials. Application as Catalysts for Transesterification. *Chem. Eng. J.* 2011, *166*(2), 744–750. DOI: 10.1016/j.cej.2010.11.081.

[48] Harada, K.; Sugise, R.; Kashiwagi, K.; Imbe, Y.; Doi, T.; Ishihira, K.; Shuji, T.; Ii, H. Process for Preparing Diaryl Carbonate. 1997, US Patent 5892089.

[49] Chalk, P. M.; Craswell, E. T.; Polidoro, J. C.; Chen, D. Fate and Efficiency of ^{15}N-Labelled Slow- and Controlled-Release Fertilizers. *Nutr. Cycl. Agroecosyst.* 2015, *102*, 167–178. DOI: 10.1007/s10705-015-9697-2.

[50] Zheng, W.; Papiernik, S. K.; Guo, M.; Yates, S. R. Accelerated Degradation of Methyl Iodide by Agrochemicals. *J. Agric. Food Chem.* 2003, *51*(3), 673–679. DOI: 10.1021/jf020820q.

[51] Mancuso, R.; Raut, D. S.; Della Ca', N.; Fini, F.; Carfagna, C.; Gabriele, B. Catalytic Oxidative Carbonylation of Amino Moieties to Ureas, Oxamides, 2-Oxazolidinones, and Benzoxazolones. *ChemSusChem.* 2015, *8*(13), 2204–2211. DOI: 10.1002/cssc.201500343.

[52] Messina, G.; Sechi, G. M.; De Micheli, S. Continuous Production of Oxamide by the Catalytic Oxidation of HCN. 1997, EP Patent 0571041.

[53] Mu, S.; Shang, R.; Wei, L.; Jiang, Y. Analysis on Derivatives for Coal to Ethylene Glycol Production Chain. *Mod. Chem. Ind. (China)* 2018, *38*(1), 12–17. DOI: 10.16606/j.cnki.issn0253-4320.2018.01.003.

[54] Costa, R. S.; Aranha, B. S. R.; Ghosh, A.; Lobo, A. O.; Da Silva, E. T. S. G.; Alves, D. C. B.; Viana, B. C. Production of Oxalic Acid by Electrochemical

Reduction of CO_2 Using Silver-Carbon Material from Babassu Coconut Mesocarp. *J. Phys. Chem. Solids.* 2020, *147*, 109678. DOI: 10.1016/j.jpcs.2020.109678.

[55] Li, A.; Li, Y.; Geng, S.; Song, P. Production Methods for Oxalic Acid. *Coal Chem. Ind. (China)* 2006, *126*, 58–60.

[56] Xu, Y.; Chen, Q.; Zhao, Y.; Lv, J.; Li, Z.; Ma, X. Autocatalytic Kinetic Study of Dimethyl Oxalate Consecutive Hydrolysis. *Ind. Eng. Chem. Res.* 2014, *53*(11), 4207–4214. DOI: 10.1021/ie404253x.

[57] Pawar, A. A.; Lee, D.; Chung, W.; Kim, H. Understanding the Synergy between MgO-CeO_2 as an Effective Promoter and Ionic Liquids for High Dimethyl Carbonate Production from CO_2 and Methanol. *Chem. Eng. J.* 2020, *395*, 124970. DOI: 10.1016/j.cej.2020.124970.

[58] Fiorani, G.; Perosa, A.; Selva, M. Dimethyl Carbonate: A Versatile Reagent for a Sustainable Valorization of Renewables. *Green Chem.* 2018, *20*(2), 288–322. DOI: 10.1039/C7GC02118F.

[59] Kumar, P.; Srivastava, V. C.; Štangar, U. L.; Mušič, B.; Mishra, I. M.; Meng, Y. Recent Progress in Dimethyl Carbonate Synthesis Using Different Feedstock and Techniques in the Presence of Heterogeneous Catalysts. *Catal. Rev.* 2021, *63*(3), 363–421. DOI: 10.1080/01614940.2019.1696609.

[60] Wang, C.; Xu, N.; Liu, T.; Xu, W.; Guo, H.; Li, Y.; Bai, P.; Wu, X.; Gong, X.; Liu, X.; Mintova, S. Mechanical Pressure-Mediated Pd Active Sites Formation in NaY Zeolite Catalysts for Indirect Oxidative Carbonylation of Methanol to Dimethyl Carbonate. *J. Catal.* 2021, *396*, 269–280. DOI: 10.1016/j.jcat.2021.03.009.

[61] Huang, S.; Yan, B.; Wang, S.; Ma, X. Recent Advances in Dialkyl Carbonates Synthesis and Applications. *Chem. Soc. Rev.* 2015, *44*(10), 3079–3116. DOI: 10.1039/C4CS00374H.

[62] Tan, H.; Chen, Z.; Xu, Z.; Sun, J.; Wang, Z.; Si, R.; Zhuang, W.; Guo, G. Synthesis of High-Performance and High-Stability Pd(II)/NaY Catalyst for CO Direct Selective Conversion to Dimethyl Carbonate by Rational Design. *ACS Catal.* 2019, *9*(4), 3595–3603. DOI: 10.1021/acscatal.9b00286.

[63] Tan, H.; Wang, Z.; Xu, Z.; Sun, J.; Xu, Y.; Chen, Q.; Chen, Y.; Guo, G. Review on the Synthesis of Dimethyl Carbonate. *Catal. Today.* 2018, *316*, 2–12. DOI: 10.1016/j.cattod.2018.02.021.

[64] Wang, C.; Liu, B.; Liu, P.; Huang, K.; Xu, N.; Guo, H.; Bai, P.; Ling, L.; Liu, X.; Mintova, S. Elucidation of the Reaction Mechanism of Indirect Oxidative Carbonylation of Methanol to Dimethyl Carbonate on Pd/NaY Catalyst: Direct Identification of Reaction Intermediates. *J. Catal.* 2022, *412*, 30–41. DOI: 10.1016/j.jcat.2022.06.002.

[65] Hao, C.; Wang, S.; Ma, X. Thermodynamics Analysis of the Preparation of Dialkyl Carbonates from Dialkyl Oxalates by Gaseous Decarbonylation. *Specia. Petrochem. (China)* 2006, *23*(4), 36–39.

[66] Fenton, D. M.; Anahim; Steinwand, P. J. Preparation of Oxalates. 1968, US Patent 3393136.

[67] Yu, B.; Chung, C.; Chien, I. Development of a Plant-Wide Dimethyl Oxalate (DMO) Synthesis Process from Syngas: Rigorous Design and Optimization. *Comput. Chem. Eng.* 2018, *119*, 85–100. DOI: 10.1016/j.compchemeng.2018.08.025.

[68] Cassady, C. J.; Freiser, B. S. Gas-Phase Reactions of Transition-Metal Ions with Methyl Nitrite and Nitromethane. *J. Am. Chem. Soc.* 1985, *107*(6), 1566–1573. DOI: 10.1021/ja00292a019.

[69] Gao, Z.; Liu, Z.; He, F.; Xu, G. Combined XPS and in Situ DRIRS Study of Mechanism of Pd-Fe/α-Al_2O_3 Catalyzed CO Coupling Reaction to Diethyl Oxalate. *J. Mol. Catal. A: Chem.* 2005, *235*(1–2), 143–149. DOI: 10.1016/j.molcata.2005.03.003.

[70] Ji, Y.; Liu, G.; Li, W.; Xiao, W. The Mechanism of CO Coupling Reaction to Form Dimethyl Oxalate over Pd/α-Al_2O_3. *J. Mol. Catal. A: Chem.* 2009, *314*(1–2), 63–70. DOI: 10.1016/j.molcata.2009.08.018.

[71] Zhai, H.; Wang, S.; Chen, D.; Cheng, X.; Xie, C. Research on Thermal Risk and Decomposition Behavior of Methyl Nitrite. *Chin. J. Chem. Eng.* 2020, *28*(8), 2131–2136. DOI: 10.1016/j.cjche.2020.05.031.

[72] Wang, C.; Xu, W.; Qin, Z.; Guo, H.; Liu, X.; Mintova, S. Highly Active Pd Containing EMT Zeolite Catalyst for Indirect Oxidative Carbonylation of Methanol to Dimethyl Carbonate. *J. Energy Chem.* 2021, *52*, 191–201. DOI: 10.1016/j.jechem.2020.04.045.

[73] Tahara, S.; Fujii, K.; Nishihira, K.; Matsuda, M.; Mizutare, K. Process for Continuous Preparation of Diester of Oxalic Acid, 1984, US Patent 4407109.

[74] Liu, X.; Ji, Y.; Li, W.; Xiao, W. Preparation and Catalytic Activity of Egg-Shelled Catalyst Pd/α-Al_2O_3. *Chin. J. Catal.* 2009, *30*(3), 213–217. DOI: 0253-9837(2009)03-0213-05.

[75] Peng, S.; Xu, Z.; Chen, Q.; Wang, Z.; Lv, D.; Sun, J.; Chen, Y.; Guo, G. Enhanced Stability of Pd/ZnO Catalyst for CO Oxidative Coupling to Dimethyl Oxalate: Effect of Mg^{2+} Doping. *ACS Catal.* 2015, *5*(7), 4410–4417. DOI: 10.1021/acscatal.5b00365.

[76] Peng, S.; Xu, Z.; Chen, Q.; Wang, Z.; Chen, Y.; Lv, D.; Lu, G.; Guo, G. MgO: An Excellent Catalyst Support for CO Oxidative Coupling to Dimethyl Oxalate. *Catal. Sci. Technol.* 2014, *4*(7), 1925–1930. DOI: 10.1039/C4CY00245H.

[77] Zhao, T.; Chen, D.; Dai, Y.; Yuan, W.; Holmen, A. Synthesis of Dimethyl Oxalate from CO and CH_3ONO on Carbon Nanofiber Supported Palladium Catalysts. *Ind. Eng. Chem. Res.* 2004, *43*(16), 4595–4601. DOI: 10.1021/ie030728z.

[78] Jin, E.; He, L.; Zhang, Y.; Richard, A. R.; Fan, M. A Nanostructured CeO_2 Promoted Pd/α-Alumina Diethyl Oxalate Catalyst with High Activity and Stability. *RSC Adv.* 2014, *4*(90), 48901–48904. DOI: 10.1039/C4RA08170F.

[79] Zhao, X.; Lin, Q.; Xiao, W. Characterization of Pd-CeO_2/α-Alumina Catalyst for Synthesis of Dimethyl Oxalate. *Appl. Catal. A.* 2005, *284*(1–2), 253–257. DOI: 10.1016/j.apcata.2005.02.004.

[80] Wang, S.; Zhang, X.; Zhao, Y.; Ge, Y.; Lv, J.; Wang, B.; Ma, X. Pd-Fe/α-Al_2O_3/Cordierite Monolithic Catalysts for the Synthesis of Dimethyl Oxalate: Effects of Calcination and Structure. *Front. Chem. Sci. Eng.* 2012, *6*, 259–269. DOI: 10.1007/s11705-012-1212-6.

[81] Gao, X.; Zhao, Y.; Wang, S.; Yin, Y.; Wang, B.; Ma, X. A Pd-Fe/α-Al_2O_3/Cordierite Monolithic Catalyst for CO Coupling to Oxalate. *Chem. Eng. Sci.* 2011, *66*(15), 3513–3522. DOI: 10.1016/j.ces.2011.04.012.

[82] Wang, C.; Ding, J.; Zhao, G.; Deng, T.; Liu, Y.; Lu, Y. Microfibrous-Structured Pd/AlOOH/Al-Fiber for CO Coupling to Dimethyl Oxalate: Effect of Morphology of AlOOH Nanosheet Endogenously Grown on Al-Fiber. *ACS Appl. Mater. Interfaces.* 2017, *9*(11), 9795–9804. DOI: 10.1021/acsami.7b00889.

[83] Wang, C.; Jia, Y.; Zhang, Z.; Zhao, G.; Liu, Y.; Lu, Y. Role of PdC_x Species in Pd@PdC_x/AlOOH/Al-Fiber Catalyst for the CO Oxidative Coupling to Dimethyl

Oxalate. *Appl. Surf. Sci.* 2019, *478*(1), 840–845. DOI: 10.1016/j.apsusc.2019.02.031.

[84] Wang, C.; Xu, W.; Qin, Z.; Liu, X.; Mintova, S. Low-Temperature Synthesis of α-Alumina Nanosheets on Microfibrous-Structured Al-Fibers for Pd-Catalyzed CO Oxidative Coupling to Dimethyl Oxalate. *Catal. Today.* 2020, *354*(1), 158–166. DOI: 10.1016/j.cattod.2019.03.005.

[85] Wang, C.; Xu, W.; Qin, Z.; Mintova, S. Spontaneous Galvanic Deposition of Nanoporous Pd on Microfibrous-Structured Al-Fibers for CO Oxidative Coupling to Dimethyl Oxalate. *Catal. Commun.* 2019, *119*, 39–41. DOI: 10.1016/j.catcom.2018.10.014.

[86] Tan, H.; Chen, Z.; Jing, K.; Sun, J.; Xu, Y.; Zhang, N.; Xu, Z.; Guo, G. Paired-Pd(II) Centers Embedded in HKUST-1 Framework: Tuning the Selectivity from Dimethyl Carbonate to Dimethyl Oxalate. *J. Energy Chem.* 2022, *67*, 233–240. DOI: 10.1016/j.jechem.2021.09.033.

[87] Jing, K.; Fu, Y.; Chen, Z.; Zhang, T.; Sun, J.; Xu, Z.; Guo, G. Boosting Interfacial Electron Transfer between Pd and ZnTi-LDH via Defect Induction for Enhanced Metal-Support Interaction in CO Direct Esterification Reaction. *ACS Appl. Mater. Interfaces.* 2021, *13*(21), 24856–24864. DOI: 10.1021/acsami.1c04523.

[88] Zhang, Z.; Lin, X.; Jiang, H.; Yang, Z.; Xu, Y.; Sun, J.; Xu, Z.; Guo, G. Enhancing the Activity of Pd/Zn-Al-O Catalysts for Esterification of CO to Dimethyl Oxalate via Increasing Oxygen Defects by Tuning the Zn/Al Ratio. *Catal. Sci. Technol.* 2022, *12*(13), 4273–4280. DOI: 10.1039/D2CY00369D.

[89] Tan, H.; Xu, Y.; Rong, S.; Zhao, R.; Cui, H.; Chen, Z.; Xu, Z.; Zhang, N.; Guo, G. Enhanced Metal-Support Interaction between Pd and Hierarchical Nb_2O_5 via Oxygen Defect Induction to Promote CO Oxidative Coupling to Dimethyl Oxalate. *Nanoscale.* 2021, *13*(44), 18773–18779. DOI: 10.1039/D1NR03370K.

[90] Yang, L.; Pan, Z.; Wang, D.; Wang, S.; Wang, X.; Ma, H.; Liu, H.; Wang, C.; Qu, W.; Tian, Z. Highly Effective Pd/MgO/γ-Al_2O_3 Catalysts for CO Oxidative Coupling to Dimethyl Oxalate: The Effect of MgO Coating on γ-Al_2O_3. *ACS Appl. Mater. Interfaces.* 2021, *13*(24), 28064–28071. DOI: 10.1021/acsami.1c04051.

[91] Yang, L.; Pan, Z.; Wang, D.; Wang, S.; Wang, X.; Ma, H.; Qu, W.; Tian, Z. Mechanochemical Synthesis of a High-Surface-Area Pd/α-Al_2O_3 Catalyst for CO

Oxidative Coupling to Dimethyl Oxalate Reaction. *Catal. Sci. Technol.* 2023, *13*(13), 3796−3803. DOI: 10.1039/D2CY01895K.

[92] Hu, S.; Xie, C.; Xu, Y.; Chen, X.; Gao, M.; Wang, H.; Yang, W.; Xu, Z.; Guo, G.; Jiang, H. Selectivity Control in the Direct CO Esterification over Pd@UiO-66: The Pd Location Matters. *Angew. Chem. Int. Ed.* 2023, *62*, e202311625. DOI: 10.1002/anie.202311625.

[93] Wang, C.; Chen, P.; Li, Y.; Zhao, G.; Liu, Y.; Lu, Y. In Situ DRIFTS Study of CO Coupling to Dimethyl Oxalate over Structured Al-Fiber@ns-AlOOH@Pd Catalyst. *J. Catal.* 2016, *344*, 173−183. DOI: 10.1016/j.jcat.2016.09.031.

[94] Wang, C.; Han, L.; Zhang, Q.; Li, Y.; Zhao, G.; Liu, Y.; Lu, Y. Endogenous Growth of 2D AlOOH Nanosheets on a 3D Al-Fiber Network via Steam-Only Oxidation in Application for Forming Structured Catalysts. *Green Chem.* 2015, *17*(7), 3762−3765. DOI: 10.1039/C5GC00530B.

[95] Lang, R.; Du, X.; Huang, Y.; Jiang, X.; Zhang, Q.; Guo, Y.; Liu, K.; Qiao, B.; Wang, A.; Zhang, T. Single-Atom Catalysts Based on the Metal-Oxide Interaction. *Chem. Rev.* 2020, *120*(21), 11986−12043. DOI: 10.1021/acs.chemrev.0c00797.

[96] Hannagan, R. T.; Giannakakis, G.; Flytzani-Stephanopoulos, M.; Sykes, E. C. H. Single-Atom Alloy Catalysis. *Chem. Rev.* 2020, *120*(21), 12044−12088. DOI: 10.1021/acs.chemrev.0c00078.

[97] Babucci, M.; Guntida, A.; Gates, B. C. Atomically Dispersed Metals on Well-Defined Supports Including Zeolites and Metal-Organic Frameworks: Structure, Bonding, Reactivity, and Catalysis. *Chem. Rev.* 2020, *120*(21), 11956−11985. DOI: 10.1021/acs.chemrev.0c00864.

[98] Ling, L.; Feng, X.; Cao, Y.; Liu, P.; Fan, M.; Zhang, R.; Wang, B. The Catalytic CO Oxidative Coupling to Dimethyl Oxalate on Pd Clusters Anchored on Defected Graphene: A Theoretical Study. *Mol. Catal.* 2018, *453*, 100−112. DOI: 10.1016/j.mcat.2018.04.021.

[99] Ling, L.; Cao, Y.; Han, M.; Liu, P.; Zhang, R.; Wang, B. Catalytic Performance of Pd_n (n = 1, 2, 3, 4 and 6) Clusters Supported on TiO_{2-V} for the Formation of Dimethyl Oxalate via the CO Catalytic Coupling Reaction: A Theoretical Study. *Phys. Chem. Chem. Phys.* 2020, *22*(8), 4549−4560. DOI: 10.1039/C9CP06773F.

[100] Zhang, T.; Walsh, A. G.; Yu, J.; Zhang, P. Single-Atom Alloy Catalysts: Structural Analysis, Electronic Properties and Catalytic Activities. *Chem. Soc. Rev.* 2021, *50*(1), 569–588. DOI: 10.1039/D0CS00844C.

[101] Li, Z.; Ji, S.; Liu, Y.; Cao, X.; Tian, S.; Chen, Y.; Niu, Z.; Li, Y. Well-Defined Materials for Heterogeneous Catalysis: From Nanoparticles to Isolated Single-Atom Sites. *Chem. Rev.* 2020, *120*(2), 623–682. DOI: 10.1021/acs.chemrev.9b00311.

[102] Qu, Y.; Wang, Y.; Li, J.; Xu, Q.; Liang, X.; Jiang, A. Insights into the Pd Nanocatalysts Directed by Morphology Effect for CO and Methyl Nitrite Coupling to Dimethyl Oxalate. *Mol. Catal.* 2020, *490*, 110949. DOI: 10.1016/j.mcat.2020.110949.

[103] Kaiser, S. K.; Chen, Z.; Faust Akl, D.; Mitchell, S.; Pérez-Ramírez, J. Single-Atom Catalysts across the Periodic Table. *Chem. Rev.* 2020, *120*(21), 11703–11809. DOI: 10.1021/acs.chemrev.0c00576.

[104] Wang, X.; Li, Z.; Qu, Y.; Yuan, T.; Wang, W.; Wu, Y.; Li, Y. Review of Metal Catalysts for Oxygen Reduction Reaction: From Nanoscale Engineering to Atomic Design. *Chem.* 2019, *5*(6), 1486–1511. DOI: 10.1016/j.chempr.2019.03.002.

[105] Tengco, J. M. M.; Lugo-José, Y. K.; Monnier, J. R.; Regalbuto, J. R. Chemisorption-XRD Particle Size Discrepancy of Carbon Supported Palladium: Carbon Decoration of Pd? *Catal. Today.* 2015, *246*, 9–14. DOI: 10.1016/j.cattod.2014.07.006.

[106] Krishnankutty, N.; Vannice, M. A. The Effect of Pretreatment on Pd/C Catalysts: I. Adsorption and Absorption Properties. *J. Catal.* 1995, *155*(2), 312–326. DOI: 10.1006/jcat.1995.1213.

[107] Liu, X.; Ji, Y.; Li, W.; Xiao, W. Preparation and Catalytic Activity of Egg-Shelled Catalyst Pd/α-Al_2O_3. *Chin. J. Catal.* 2009, *30*(3), 213–217.

[108] Han, B.; Ling, L.; Zhang, R.; Liu, P.; Fan, M.; Wang, B. Dimethyl Oxalate Synthesis via CO Oxidation on Pd-Doped Ag(111) Surface: A Theoretic Study. *Mol. Catal.* 2020, *484*, 110731. DOI: 10.1016/j.mcat.2019.110731.

[109] Han, B.; Ling, L.; Fan, M.; Liu, P.; Wang, B.; Zhang, R. A DFT Study and Microkinetic Analysis of CO Oxidation to Dimethyl Oxalate over Pd Stripe and Pd Single Atom-Doped Cu(111) Surfaces. *Appl. Surf. Sci.* 2019, *479*, 1057–1067. DOI: 10.1016/j.apsusc.2019.02.112.

[110] Zhao, J.; Yin, L.; Ling, L.; Zhang, R.; Fan, M.; Wang, B. A Predicted New Catalyst to Replace Noble Metal Pd for CO Oxidative Coupling to DMO. Catal. Sci. Technol. 2022, 12(8), 2542−2554. DOI: 10.1039/D1CY01631H.

[111] Zhuo, G.; Jiang, X. Catalytic Decomposition of Ethyl Nitrite over Supported Palladium Catalyst. *Chin. J. Catal.* 2003, *24*(7), 509−512.

[112] Li, Z.; Wang, W.; Yin, D.; Lv, J.; Ma, X. Effect of Alkyl Nitrite Decomposition on Catalytic Performance of CO Coupling Reaction over Supported Palladium Catalyst. *Front. Chem. Sci. Eng.* 2012, *6*, 410−414. DOI: 10.1007/s11705-012-1213-5.

[113] Rahmati, M.; Huang, B.; Mortensen, M. K.; Keyvanloo, K.; Fletcher, T. H.; Woodfield, B. F.; Hecker, W. C.; Argyle, M. D. Effect of Different Alumina Supports on Performance of Cobalt Fischer-Tropsch Catalysts. *J. Catal*. 2018, *359*, 92−100. DOI: 10.1016/j.jcat.2017.12.022.

[114] van den Reijen, J. E.; Kanungo, S.; Welling, T. A. J.; Versluijs-Helder, M.; Nijhuis, T. A.; de Jong, K. P.; de Jongh, P. E. Preparation and Particle Size Effects of Ag/α-Al_2O_3 Catalysts for Ethylene Epoxidation. *J. Catal*. 2017, *356*, 65−74. DOI: 10.1016/j.jcat.2017.10.001.

[115] Ji, S.; Chen, Y.; Wang, X.; Zhang, Z.; Wang, D.; Li, Y. Chemical Synthesis of Single Atomic Site Catalysts. *Chem. Rev.* 2020, *120*(21), 11900−11955. DOI: 10.1021/acs.chemrev.9b00818.

[116] Cao, Y.; Ling, L.; Lin, H.; Fan, M.; Liu, P.; Zhang, R.; Wang, B. DFT Study on CO Oxidative Coupling to DMO over Pd_4/TiO_2 and Pd_4/TiO_2-O_v: A Role of Oxygen Vacancy on Support. *Comput. Mater. Sci.* 2019, *159*, 1−11. DOI: 10.1016/j.commatsci.2018.11.047.

[117] Huang, Y.; Pan, P.; Li, Q.; Han, B.; Ye, R.; Yao, Y. Regulating the Metal-Support Interactions by Tuning the Ratios between N and B Based on the C_2N Motif to Develop Efficient Pd-Based Catalysts for CO Oxidative Coupling to DMO: A DFT Study. *Appl. Surf. Sci.* 2023, *614*, 156205. DOI: 10.1016/j.apsusc.2022.156205.

[118] Lin, S.; Xu, Z.; Lin, J.; Guo, G. Theoretical Exploration of the Origin of Selectivity for the Oxidative Carbonylation Reaction Catalyzed by a Single Pd Atom Embedded on Graphene. *Catal. Sci. Technol.* 2023, *13*(8), 2421−2431. DOI: 10.1039/D3CY00091E.

[119] Li, L.; Chang, X.; Lin, X.; Zhao, Z. J.; Gong, J. Theoretical Insights into Single-Atom Catalysts. *Chem. Soc. Rev.* 2020, *49*(22), 8156–8178. DOI: 10.1039/D0CS00795A.

[120] Le, S. D.; Nishimura, S. Effect of Support on the Formation of CuPd Alloy Nanoparticles for the Hydrogenation of Succinic Acid. *Appl. Catal. B.* 2021, *282*, 119619. DOI: 10.1016/j.apcatb.2020.119619.

[121] Dong, J.; Fu, Q.; Li, H.; Xiao, J.; Yang, B.; Zhang, B.; Bai, Y.; Song, T.; Zhang, R.; Gao, L.; Cai, J.; Zhang, H.; Liu, Z.; Bao, X. Reaction-Induced Strong Metal-Support Interactions between Metals and Inert Boron Nitride Nanosheets. *J. Am. Chem. Soc.* 2020, *142*(40), 17167–17174. DOI: 10.1021/jacs.0c08139.

[122] Ham, H.; Baek, S. W.; Shin, C.; Bae, J. W. Roles of Structural Promoters for Direct CO_2 Hydrogenation to Dimethyl Ether over Ordered Mesoporous Bifunctional Cu/M-Al_2O_3 (M = Ga or Zn). *ACS Catal.* 2019, *9*(1), 679–690. DOI: 10.1021/acscatal.8b04060.

[123] Dong, Y.; Shen, Y.; Zhao, Y.; Wang, S.; Ma, X. Synergy between Palladium and Potassium Species for Efficient Activation of Carbon Monoxide in the Synthesis of Dimethyl Carbonate. *ChemCatChem.* 2015, *7*(16), 2460–2466. DOI: 10.1002/cctc.201500317.

[124] Gao, Z.; Hu, C.; Li, Z.; He, F.; Xu, G. Surface Structure of Pd-Fe/α-Al_2O_3 Catalyst for CO Coupling to Diethyl Oxalate. *Chin. J. Catal.* 2004, *25*(3), 205–209.

[125] Zhao, X. G.; Lu, X. L.; Zhao, H. G.; Zhu, Y. Q.; Xiao, W. D. Study on Pd/α-Al_2O_3 Catalyst for Vapor-Phase Coupling Reaction of CO with CH_3ONO to $(COOCH_3)_2$. *Chin. J. Catal.* 2004, *25*(2), 125–128.

[126] Studt, F.; Sharafutdinov, I.; Abild-Pedersen, F.; Elkjær, C. F.; Hummelshøj, J. S.; Dahl, S.; Chorkendorff, I.; Nørskov, J. K. Discovery of a Ni-Ga Catalyst for Carbon Dioxide Reduction to Methanol. *Nat. Chem.* 2014, *6*(4), 320–324. DOI: 10.1038/nchem.1873.

[127] Bobadilla, L. F.; Santos, J. L.; Ivanova, S.; Odriozola, J. A.; Urakawa, A. Unravelling the Role of Oxygen Vacancies in the Mechanism of the Reverse Water-Gas Shift Reaction Byoperando DRIFTS and Ultraviolet-Visible Spectroscopy. *ACS Catal.* 2018, *8*(8), 7455–7467. DOI: 10.1021/acscatal.8b02121.

[128] Liao, X.; Liu, Y.; Chu, W.; Sall, S.; Petit, C.; Pitchon, V.; Caps, V. Promoting Effect of AuCu Alloying on Au-Cu/CeO_2-Catalyzed CO Oxidation: A Combined Kinetic and in Situ DRIFTS Study. *J. Catal.* 2020, *382*, 329–338. DOI: 10.1016/j.jcat.2019.12.029.

[129] Kijlstra, W. S.; Brands, D. S.; Poels, E. K.; Bliek, A. Mechanism of the Selective Catalytic Reduction of NO by NH_3 over MnO_x/Al_2O_3. *J. Catal.* 1997, *171*(1), 219–230. DOI: 10.1006/jcat.1997.1788.

[130] Meunier, F. C.; Breen, J. P.; Zuzaniuk, V.; Olsson, M.; Ross, J. R. H. Mechanistic Aspects of the Selective Reduction of NO by Propene over Alumina and Silver-Alumina Catalysts. *J. Catal.* 1999, *187*(2), 493–505. DOI: 10.1006/jcat.1999.2622.

[131] Fan, C.; Luo, M.; Xiao, W. Reaction Mechanism of Methyl Nitrite Dissociation During CO Catalytic Coupling to Dimethyl Oxalate: A Density Functional Theory Study. *Chin. J. Chem. Eng.* 2016, *24*(1), 132–139. DOI: 10.1016/j.cjche.2015.06.007.

[132] Li, Q.; Zhou, Z.; Chen, R.; Sun, B.; Qiao, L.; Yao, Y.; Wu, K. Insights into the Reaction Mechanism of CO Oxidative Coupling to Dimethyl Oxalate over Palladium: A Combined DFT and IR Study. *Phys. Chem. Chem. Phys.* 2015, *17*(14), 9126–9134. DOI: 10.1039/C4CP05738D.

[133] Feng, X.; Ling, L.; Cao, Y.; Zhang, R.; Fan, M.; Wang, B. A DFT Study on the Catalytic CO Oxidative Coupling to Dimethyl Oxalate on Al-Doped Core-Shell Pd Clusters. *J. Phys. Chem. C.* 2018, *122*(2), 1169–1179. DOI: 10.1021/acs.jpcc.7b09272.

[134] Lamberti, C.; Zecchina, A.; Groppo, E.; Bordiga, S. Probing the Surfaces of Heterogeneous Catalysts by in Situ IR Spectroscopy. *Chem. Soc. Rev.* 2010, *39*(12), 4951–5001. DOI: 10.1039/C0CS00117A.

[135] Tian, X.; Zahid, M.; Li, J.; Sun, W.; Niu, X.; Zhu, Y. Pd/Mo_2N-TiO_2 as Efficient Catalysts for Promoted Selective Hydrogenation of 4-Nitrophenol: A Green Bio-Reducing Preparation Method. *J. Catal.* 2020, *391*, 190–201. DOI: 10.1016/j.jcat.2020.08.027.

[136] Tan, T. H.; Xie, B.; Ng, Y. H.; Abdullah, S. F. B.; Tang, H. Y. M.; Bedford, N.; Taylor, R. A.; Aguey-Zinsou, K.; Amal, R.; Scott, J. Unlocking the Potential of the Formate Pathway in the Photo-Assisted Sabatier Reaction. *Nat. Catal.* 2020, *3*(12), 1034–1043. DOI: 10.1038/s41929-020-00544-3.

[137] Wang, Y.; Duan, X.; Xie, Y.; Sun, H.; Wang, S. Nanocarbon-Based Catalytic Ozonation for Aqueous Oxidation: Engineering Defects for Active Sites and Tunable Reaction Pathways. *ACS Catal.* 2020, *10*(22), 13383−13414. DOI: 10.1021/acscatal.0c04232.

[138] Waller, F. J. Recent Achievements, Trends and Prospects in Homogeneous Catalysis. *J. Mol. Catal.* 1985, *31*(2), 123−136. DOI: 10.1016/0304-5102(85)85054-9.

[139] Han, B.; Feng, X.; Ling, L.; Fan, M.; Liu, P.; Zhang, R.; Wang, B. CO Oxidative Coupling to Dimethyl Oxalate over Pd-Me (Me = Cu, Al) Catalysts: A Combined DFT and Kinetic Study. *Phys. Chem. Chem. Phys.* 2018, *20*(10), 7317−7332. DOI: 10.1039/c7cp08306h.

[140] Kiani, D.; Sourav, S.; Tang, Y.; Baltrusaitis, J.; Wachs, I. E. Methane Activation by ZSM-5-Supported Transition Metal Centers. *Chem. Soc. Rev.* 2021, *50*(2), 1251−1268. DOI: 10.1039/D0CS01016B.

[141] Meng, F.; Xu, G.; Guo, R.; Yan, H.; Chen, M. Kinetic Study of Carbon Monoxide Coupling Reaction over Supported Palladium Catalyst. *Chem. Eng. Process.* 2004, *43*(6), 785−790. DOI: 10.1016/S0255-2701(03)00082-5.

[142] Meng, F.; Xu, G.; Guo, Q. Kinetics of the Catalytic Coupling Reaction of Carbon Monoxide to Diethyl Oxalate over Pd-Fe/α-Al_2O_3 Catalyst. *J. Mol. Catal. A: Chem.* 2003, *201*(1-2), 283−288. DOI: 10.1016/S1381-1169(03)00182-1.

[143] Motagamwala, A. H.; Dumesic, J. A. Microkinetic Modeling: A Tool for Rational Catalyst Design. *Chem. Rev.* 2021, *121*(2), 1049−1076. DOI: 10.1021/acs.chemrev.0c00394.

[144] Prašnikar, A.; Jurković, D. L.; Likozar, B. Reaction Path Analysis of CO_2 Reduction to Methanol through Multisite Microkinetic Modelling over Cu/ZnO/Al_2O_3 Catalysts. *Appl. Catal. B.* 2021, *292*, 120190. DOI: 10.1016/j.apcatb.2021.120190.

[145] Ma, H.; Schneider, W. F. DFT and Microkinetic Comparison of Pt, Pd and Rh-Catalyzed Ammonia Oxidation. *J. Catal.* 2020, *383*, 322−330. DOI: 10.1016/j.jcat.2020.01.029.

[146] Xie, W.; Xu, J.; Ding, Y.; Hu, P. Quantitative Studies of the Key Aspects in Selective Acetylene Hydrogenation on Pd(111) by Microkinetic Modeling with

Coverage Effects and Molecular Dynamics. *ACS Catal.* 2021, *11*(7), 4094−4106. DOI: 10.1021/acscatal.0c05345.

[147] Ishikawa, A.; Tateyama, Y. A First-Principles Microkinetics for Homogeneous-Heterogeneous Reactions: Application to Oxidative Coupling of Methane Catalyzed by Magnesium Oxide. *ACS Catal.* 2021, *11*(5), 2691−2700. DOI: 10.1021/acscatal.0c04104.

[148] Zheng, M.; Zhao, L.; Cao, L.; Gao, J.; Xu, C. The Combined DFT and Microkinetics Methods to Investigate the Favorite Sulfur Vacancies of CO(Ni)MoS_2 Catalysts for Maximizing HDS/HYDO Selectivity. *Appl. Catal. B.* 2020, *277*, 119242. DOI: 10.1016/j.apcatb.2020.119242.

[149] Ling, L.; Lin, H.; Han, B.; Liu, P.; Zhang, R.; Wang, B. Insight into the Effect of Surface Structure for Pd Catalyst on CO Oxidative Coupling to Dimethyl Oxalate. *Mol. Catal.* 2019, *470*, 19−31. DOI: 10.1016/j.mcat.2019.03.017.

[150] Han, B.; Lin, H.; Ling, L.; Liu, P.; Fan, M.; Wang, B.; Zhang, R. A DFT Study on Dimethyl Oxalate Synthesis over Pd_{ML}/Ni(111) and Pd_{ML}/Co(111) Surfaces. *Appl. Surf. Sci.* 2019, *465*, 498−508. DOI: 10.1016/j.apsusc.2018.09.152.

[151] Mitchell, S.; Michels, N.; Pérez-Ramírez, J. From Powder to Technical Body: The Undervalued Science of Catalyst Scale Up. *Chem. Soc. Rev.* 2013, *42*(14), 6094−6112. DOI: 10.1039/c3cs60076a.

[152] Whiting, G. T.; Chung, S.; Stosic, D.; Chowdhury, A. D.; van der Wal, L. I.; Fu, D.; Zecevic, J.; Travert, A.; Houben, K.; Baldus, M.; Weckhuysen, B. M. Multiscale Mechanistic Insights of Shaped Catalyst Body Formulations and Their Impact on Catalytic Properties. *ACS Catal.* 2019, *9*(6), 4792−4803. DOI: 10.1021/acscatal.9b00151.

[153] Wahid, S.; Cahela, D. R.; Tatarchuk, B. J. Comparison of Wash-Coated Monoliths Vs. Microfibrous Entrapped Catalyst Structures for Catalytic VOC Removal. *AIChE J.* 2014, *60*(11), 3814−3823. DOI: 10.1002/aic.14555.

[154] Sheng, M.; Yang, H.; Cahela, D. R.; Yantz, W. R.; Gonzalez, C. F.; Tatarchuk, B. J. High Conductivity Catalyst Structures for Applications in Exothermic Reactions. *Appl. Catal. A.* 2012, *445–446*, 143−152. DOI: 10.1016/j.apcata.2012.08.012.

[155] Montebelli, A.; Visconti, C. G.; Groppi, G.; Tronconi, E.; Cristiani, C.; Ferreira, C.; Kohler, S. Methods for the Catalytic Activation of Metallic Structured

Substrates. *Catal. Sci. Technol.* 2014, *4*(9), 2846–2870. DOI: 10.1039/C4CY00179F.

[156] Zhao, G.; Liu, Y.; Lu, Y. Foam/Fiber-Structured Catalysts: Non-Dip-Coating Fabrication Strategy and Applications in Heterogeneous Catalysis. *Sci. Bull.* 2016, *61*, 745–748. DOI: 10.1007/s11434-016-1074-2.

[157] Parra-Cabrera, C.; Achille, C.; Kuhn, S.; Ameloot, R. 3D Printing in Chemical Engineering and Catalytic Technology: Structured Catalysts, Mixers and Reactors. *Chem. Soc. Rev.* 2018, *47*(1), 209–230. DOI: 10.1039/C7CS00631D.

[158] Lee, W.; Park, S. Porous Anodic Aluminum Oxide: Anodization and Templated Synthesis of Functional Nanostructures. *Chem. Rev.* 2014, *114*(15), 7487–7556. DOI: 10.1021/cr500002z.

[159] Balzarotti, R.; Ambrosetti, M.; Arnesano, M.; Anglani, A.; Groppi, G.; Tronconi, E. Periodic Open Cellular Structures (POCS) as Enhanced Catalyst Supports: Optimization of the Coating Procedure and Analysis of Mass Transport. *Appl. Catal. B.* 2021, *283*, 119651. DOI: 10.1016/j.apcatb.2020.119651.

[160] Lee, Y.; Cha, J.; Kwak, Y.; Park, Y.; Jo, Y. S.; Jeong, H.; Sohn, H.; Yoon, C. W.; Kim, Y.; Kim, K.; Nam, S. W. Top-Down Syntheses of Nickel-Based Structured Catalysts for Hydrogen Production from Ammonia. *ACS Appl. Mater. Interfaces.* 2021, *13*(1), 597–607. DOI: 10.1021/acsami.0c18454.

[161] Wang, S.; Zhu, J.; Si, J.; Zhao, G.; Liu, Y.; Lu, Y. High-Performance Pd/Brass-Fiber Catalyst for Selective Hydrogenation of Acetylene: Effect of Calcination-Assisted Endogenous Growth of ZnO-CuO_x on Brass-Fiber. *J. Catal.* 2020, *382*, 295–304. DOI: 10.1016/j.jcat.2019.12.027.

[162] Zhu, J.; Zhao, G.; Sun, W.; Nie, Q.; Wang, S.; Xue, Q.; Liu, Y.; Lu, Y. Superior $FeNi_3$-FeO_x/Ni-Foam Catalyst for Gas-Phase Hydrogenation of Dimethyl Oxalate to Ethanol. *Appl. Catal. B.* 2020, *270*, 118873. DOI: 10.1016/j.apcatb.2020.118873.

[163] Zhang, Z.; Zhao, G.; Sun, W.; Liu, Y.; Lu, Y. Oxidative Dehydrogenation of Ethane: Superior Nb_2O_5-NiO/Ni-Foam Catalyst Tailored by Tuning Morphology of NiO-Precursors Grown on a Ni-Foam. *iScience.* 2019, *20*, 90–99. DOI: 10.1016/j.isci.2019.09.021.

[164] Zhao, G.; Chai, R.; Zhang, Z.; Sun, W.; Liu, Y.; Lu, Y. High-Performance Ni-$CeAlO_3$-Al_2O_3/FeCrAl-Fiber Catalyst for Catalytic Oxy-Methane Reforming to Syngas. *Fuel.* 2019, *258*, 116102. DOI: 10.1016/j.fuel.2019.116102.

[165] Zhao, G.; Pan, X.; Zhang, Z.; Liu, Y.; Lu, Y. A Thin-Felt Pd-MgO-Al_2O_3/Al-Fiber Catalyst for Catalytic Combustion of Methane with Resistance to Water-Vapor Poisoning. *J. Catal.* 2020, *384*, 122–135. DOI: 10.1016/j.jcat.2020.01.013.

[166] Ding, J.; Jia, Y.; Chen, P.; Zhao, G.; Liu, Y.; Lu, Y. Thin-Felt Hollow-B-ZSM-5/SS-Fiber Catalyst for Methanol-to-Propylene: Toward Remarkable Stability Improvement from Mesoporosity-Dependent Diffusion Enhancement. *Chem. Eng. J.* 2019, *361*, 588–598. DOI: 10.1016/j.cej.2018.12.108.

[167] Kalluri, R. R.; Cahela, D. R.; Tatarchuk, B. J. Comparative Heterogeneous Contacting Efficiency in Fixed Bed Reactors: Opportunities for New Microstructured Systems. *Appl. Catal. B.* 2009, *90*(3-4), 507–515. DOI: 10.1016/j.apcatb.2009.04.015.

[168] Ambrosetti, M.; Bracconi, M.; Maestri, M.; Groppi, G.; Tronconi, E. Packed Foams for the Intensification of Catalytic Processes: Assessment of Packing Efficiency and Pressure Drop Using a Combined Experimental and Numerical Approach. *Chem. Eng. J.* 2020, *382*, 122801. DOI: 10.1016/j.cej.2019.122801.

[169] Gascon, J.; van Ommen, J. R.; Moulijn, J. A.; Kapteijn, F. Structuring Catalyst and Reactor - An Inviting Avenue to Process Intensification. *Catal. Sci. Technol.* 2015, *5*(2), 807–817. DOI: 10.1039/C4CY01406E.

[170] Porsin, A. V.; Kulikov, A. V.; Rogozhnikov, V. N.; Serkova, A. N.; Salanov, A. N.; Shefer, K. I. Structured Reactors on a Metal Mesh Catalyst for Various Applications. *Catal. Today.* 2016, *273*, 213–220. DOI: 10.1016/j.cattod.2016.03.033.

[171] Wang, W.; Tuci, G.; Duong-Viet, C.; Liu, Y.; Rossin, A.; Luconi, L.; Nhut, J.; Nguyen-Dinh, L.; Pham-Huu, C.; Giambastiani, G. Induction Heating: An Enabling Technology for the Heat Management in Catalytic Processes. *ACS Catal.* 2019, *9*(9), 7921–7935. DOI: 10.1021/acscatal.9b02471.

[172] Zenner, A.; Fiaty, K.; Bellière-Baca, V.; Rocha, C.; Gauthier, G.; Edouard, D. Effective Heat Transfers in Packed Bed: Experimental and Model Investigation. *Chem. Eng. Sci.* 2019, *201*, 424–436. DOI: 10.1016/j.ces.2019.02.028.

[173] Wei, R.; Yan, C.; Yang, A.; Shen, W.; Li, J. Improved Process Design and Optimization of 200 kt/a Ethylene Glycol Production Using Coal-Based Syngas. *Chem. Eng. Res. Des.* 2018, *132*, 551−563. DOI: 10.1016/j.cherd.2018.02.006.

[174] Mao, W.; Zheng, S.; Luo N.; Zhou J.; Gao Y.; Zhou X. Simulation and Optimization on Oxidative Coupling Reaction of CO to Dimethyl Oxalate in a Tubular Fixed Bed Reactor. *CIESC J*. 2022, *73*(1), 284−293. DOI: 10.11949/0438-1157.20211009.

[175] Chi, Z.; Liu, C.; Zhang, Y.; Li, X.; Xiao, W. Reactor Simulation and Optimization for CO Oxidative Coupling to Dimethyl Oxalate Reactions. *CIESC J*. 2022, *73*(11), 4974−4986. DOI: 10.11949/0438-1157.20220761.

[176] Zhu, Y.; Tu, S.; Luo, Z. Modeling for the Catalytic Coupling Reaction of Carbon Monoxide to Diethyl Oxalate in Fixed-Bed Reactors: Reactor Model and its Applications. *Chem. Eng. Res. Des.* 2012, *90*(9), 1361−1371. DOI: 10.1016/j.cherd.2011.12.004.

[177] Gao, X.; Zhu, Y.; Luo, Z. CFD Modeling of Gas Flow in Porous Medium and Catalytic Coupling Reaction from Carbon Monoxide to Diethyl Oxalate in Fixed-Bed Reactors. *Chem. Eng. Sci.* 2011, *66*(23), 6028−6038. DOI: 10.1016/j.ces.2011.08.031.

[178] Fang, J.; Li, Z.; Xu, G.; Wang, B.; Xiang, T. Effect of Temperature on the Deactivation of a Pd-Fe/α-Al_2O_3 Catalyst for CO Coupling to Diethyl Oxalate. *J. Energy Chem.* 2003, *12*(4), 243−246.

[179] Zhao, G.; Moulijn, J. A.; Kapteijn, F.; Dautzenberg, F. M.; Xu, B.; Lu, Y. Monolithic Fiber/Foam-Structured Catalysts: Beyond Honeycombs and Micro-Channels. *Catal. Rev.* 2023. DOI: 10.1080/01614940.2023.2240661.

[180] Pauletto, G.; Vaccari, A.; Groppi, G.; Bricaud, L.; Benito, P.; Boffito, D. C.; Lercher, J. A.; Patience, G. S. FeCrAl as a Catalyst Support. *Chem. Rev.* 2020, *120*(15), 7516−7550. DOI: 10.1021/acs.chemrev.0c00149.